Computer Modeling in Engineering & Sciences

Tech Science Press

Doi:10.32604/cmes.2025.070298

ARTICLE

A Hybrid Machine Learning and Fractional-Order Dynamical Framework for Multi-Scale Prediction of Breast Cancer Progression

David Amilo[1,*], Khadijeh Sadri[1], Evren Hincal[1,2] and Mohamed Hafez[3,4]

[1]Mathematics Research Center, Near East University TRNC, Mersin 10, Nicosia, 99138, Turkey
[2]Research Center of Applied Mathematics, Khazar University, Baku, AZ1096, Azerbaijan
[3]Department of Civil Engineering, Faculty of Engineering, FEQS INTI-IU, University, Nilai, 71800, Malaysia
[4]Faculty of Management, Shinawatra University, Pathum, 12160, Thani, Thailand

*Corresponding Author: David Amilo. Email: amilodavid.ikechukwu@neu.edu.tr

Received: 12 July 2025; Accepted: 04 September 2025; Published: 26 November 2025

ABSTRACT: Breast cancer's heterogeneous progression demands innovative tools for accurate prediction. We present a hybrid framework that integrates machine learning (ML) and fractional-order dynamics to predict tumor growth across diagnostic and temporal scales. On the Wisconsin Diagnostic Breast Cancer dataset, seven ML algorithms were evaluated, with deep neural networks (DNNs) achieving the highest accuracy (97.72%). Key morphological features (area, radius, texture, and concavity) were identified as top malignancy predictors, aligning with clinical intuition. Beyond static classification, we developed a fractional-order dynamical model using Caputo derivatives to capture memory-driven tumor progression. The model revealed clinically interpretable patterns: lower fractional orders correlated with prolonged aggressive growth, while higher orders indicated rapid stabilization, mimicking indolent subtypes. Theoretical analyses were rigorously proven, and numerical simulations closely fit clinical data. The framework's clinical utility is demonstrated through an interactive graphics user interface (GUI) that integrates real-time risk assessment with growth trajectory simulations.

KEYWORDS: Machine learning; fractional-order; breast cancer; physiological dynamics; maternal health; preventable deaths

1 Introduction

Breast cancer continues to be a major global health challenge, with complex biological behaviors that make accurate prediction of disease progression particularly difficult [1–5]. The disease's heterogeneity manifests not only in its molecular subtypes but also in its highly variable growth patterns and treatment responses [6,7]. Current diagnostic methods, while effective for detection, often struggle to provide comprehensive insights into the dynamic nature of tumor evolution [8,9]. This limitation has spurred significant interest in developing more sophisticated analytical approaches that can bridge the gap between immediate diagnostic needs and long-term prognostic predictions, particularly through the integration of computational methods with biological insights. The emergence of machine learning in medical diagnostics has revolutionized the approach to cancer classification [10–12]. These data-driven methods excel at identifying complex patterns in high-dimensional datasets, enabling highly accurate differentiation between malignant and benign lesions. Various algorithms, from traditional logistic regression to advanced deep neural networks, have demonstrated impressive performance in breast cancer diagnosis [13,14]. For instance, the study in [15] presented an AI-assisted deep learning model for early melanoma detection that

Copyright © 2025 The Authors. Published by Tech Science Press.
This work is licensed under a Creative Commons Attribution 4.0 International License, which permits unrestricted use, distribution, and reproduction in any medium, provided the original work is properly cited.

achieved high accuracy while demonstrating potential for clinical implementation. However, while these models provide excellent snapshots of disease state at a given moment, they typically cannot model the temporal dynamics of tumor progression. This represents a significant limitation, as understanding how a tumor evolves is crucial for predicting its future behavior and selecting optimal treatment strategies. The static nature of conventional machine learning approaches contrasts with the dynamic reality of cancer biology, where past states continuously influence future progression. Mathematical modeling has been instrumental in analyzing a wide range of phenomena and practical applications [16–19]. They also offer complementary strengths to machine learning by providing frameworks to simulate biological processes over time [20–22]. Traditional differential equation models have been widely used to describe tumor growth dynamics [23]; however, they often rely on simplifying assumptions that may not fully capture the complexity of real-world cancer progression. This is where fractional calculus presents an intriguing alternative. Unlike classical calculus, fractional-order models incorporate memory effects and long-range dependencies, which align well with the observed behavior of biological systems [24–26], and have shown value across multiple disciplines [27–29]. The ability to account for historical influences on current growth patterns makes fractional calculus particularly suitable for modeling cancer progression, where a tumor's past states significantly impact its future development. Recent applications of fractional-order models in biology and medicine have shown promising results, though their integration with data-driven approaches remains underexplored [30,31]. Recent advances have demonstrated the potential of combining these approaches. The authors in [32] developed a novel approach using a fractional recurrent neural network (RNN) to achieve observer-based synchronization in a fractional-order chaotic cancer cell model, while research [33] proposed a mathematical model integrated with machine learning techniques that achieved 97.65% accuracy in breast cancer prediction. Despite these advances, a critical gap remains in developing a unified framework that combines machine learning's diagnostic precision with fractional calculus's ability to model progression dynamics while maintaining clinical interpretability and utility.

Our work addresses this gap through a novel hybrid framework that begins with comprehensive machine learning analysis to identify the most predictive diagnostic features, then constructs a fractional-order dynamical system that captures the essential interactions governing tumor progression. This approach allows us to not only classify tumors with high accuracy but also to simulate their likely future behavior under different conditions. A key innovation is our use of the fractional order parameter as a potential biomarker for tumor aggressiveness, where different values correspond to distinct growth patterns observed clinically. The theoretical underpinnings of our model are rigorously developed, with careful attention to ensuring biological plausibility and clinical relevance, including proofs of existence and uniqueness of solutions. Practical implementation is achieved through a user-friendly graphical interface that integrates both classification capabilities and predictive modeling, representing a crucial step in translating complex computational methods into clinically actionable information. The broader implications of this work extend beyond breast cancer, offering a new paradigm for disease modeling that combines data-driven pattern recognition with mechanistic understanding. While advanced computational frameworks like ours aim to improve diagnostic precision, patient attitudes toward cancer management, including complementary and alternative medicine (CAM), remain critical to holistic care. Studies in low-resource settings, such as in [34], exploration of CAM perspectives among Pakistani cancer patients, reveal a gap between technological innovations and patient-centric adoption. Their findings underscore the need for culturally adaptable tools that bridge predictive analytics (like our hybrid ML-fractional model) with patient education, particularly in regions where breast cancer stigma or reliance on CAM may delay evidence-based treatment. By bridging these approaches, we move closer to truly personalized medicine, where treatment strategies can be tailored not just to a patient's current disease state but to their predicted future progression. The rest

of the paper is structured as follows: Section 2 introduces the methodology used in the study, providing the technical foundation for these advances. Section 3 details the various machine learning algorithms employed. In Section 4, the fractional-order modeling is formulated and extensively analyzed with analytic and numerical simulations. The results and implications are discussed in Section 5, while the conclusion, novelty, limitations, and future directions are given in Section 6, demonstrating the potential to transform our approach to breast cancer management.

2 Methodology

To investigate the dynamics of breast cancer progression, we developed an integrated analytical framework that combines machine learning classification with fractional-order dynamical modeling, implemented in MATLAB R2021a. This dual approach aims to leverage machine learning's strength in data-driven pattern recognition alongside fractional calculus's ability to capture memory-dependent biological processes, ensuring both predictive accuracy and biological interpretability. The methodology links machine learning outputs, such as feature importance, to the parameterization of mechanistic tumor growth models, creating a cohesive pipeline that bridges data science and mathematical biology. The dataset characteristics are summarized in Table 1, with its feature categories described in Table 2. The entire schematic flow is depicted in Fig. 1, with ultrasound image analysis illustrated in Fig. 2, showing a malignant breast tumor via diagnostic and breast ultrasound imaging, adapted from [35], highlighting irregular mass morphology, spiculated margins, and segmentation. The ML research design is illustrated in Fig. 3, with feature importance ranking and cross-validated performance metrics summarized in Tables 3 and 4, respectively. First, a comprehensive feature analysis using machine learning algorithms with the best performing algorithm, then the development of a fractional-order dynamical system informed by machine learning outputs, and finally, clinical implementation and prediction. The process begins with preprocessing the Wisconsin Diagnostic Breast Cancer dataset to ensure data quality and consistency. Subsequently, parallel workflows develop machine learning models for feature identification and fractional-order systems for tumor growth modeling. Machine learning algorithms identify key diagnostic features, which directly inform the parameterization of the fractional-order tumor growth model. This reciprocal relationship ensures that data-driven insights enhance the mechanistic understanding of cancer progression, while the fractional-order model provides interpretable dynamics grounded in biological principles. The resulting framework synthesizes empirical analysis and theoretical modeling, offering a novel paradigm for multi-scale cancer progression analysis with improved predictive performance and clinical applicability.

Table 1: Dataset overview

Property	Value
Source	UCI machine learning repository
URL	[36,37]
Number of instances	569
Number of features	30 (10 real-valued features computed for each of 3 characteristics)
Target variable	Diagnosis (Malignant/Benign)
Class distribution	37.26% malignant, 62.74% benign
Missing values	None

Table 2: Feature categories and descriptions

Feature type	Description
Radius	Mean distance from center to points on perimeter
Texture	Standard deviation of gray-scale values
Perimeter	Tumor perimeter length
Area	Tumor area
Smoothness	Local variation in radius lengths
Compactness	Perimeter^2/Area −1.0
Concavity	Severity of concave portions of contour
Concave points	Number of concave portions of contour
Symmetry	Symmetry of the tumor shape
Fractal dimension	"Coastline approximation" −1

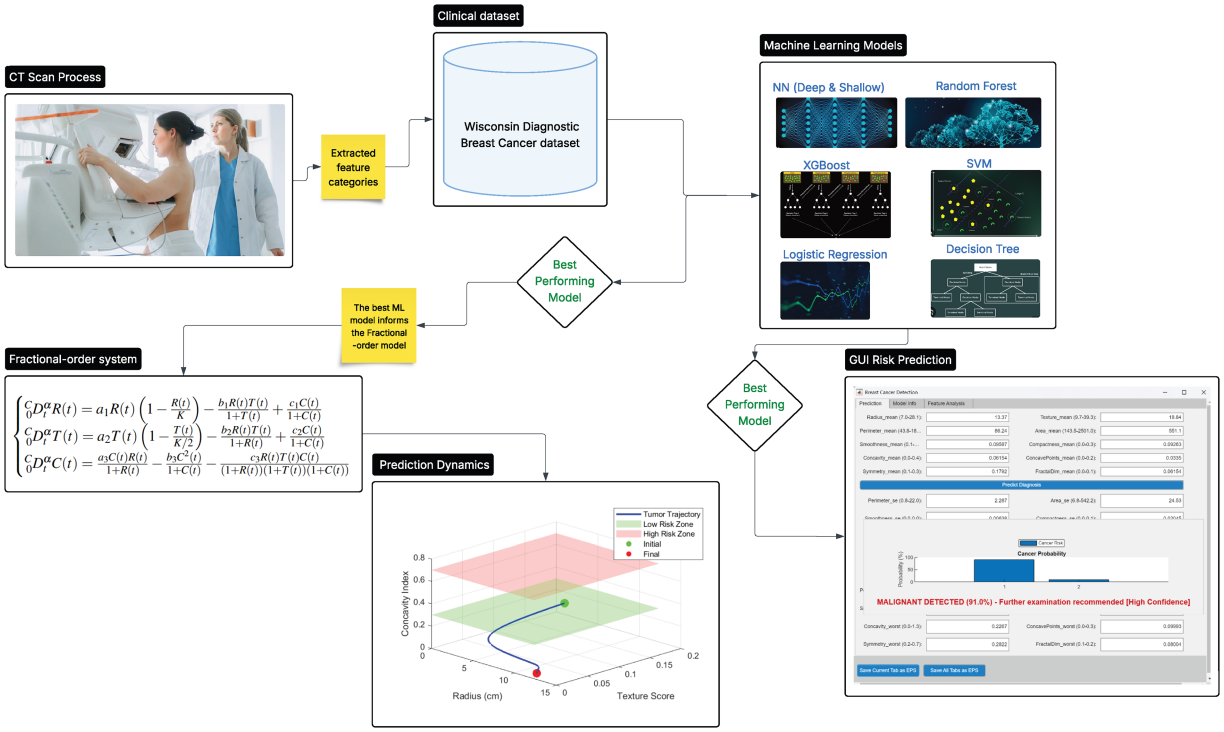

Figure 1: Schematic of the hybrid framework integrating machine learning (classification) with fractional-order dynamics (tumor progression modeling), showing bidirectional data flow between diagnostic features and growth trajectory predictions

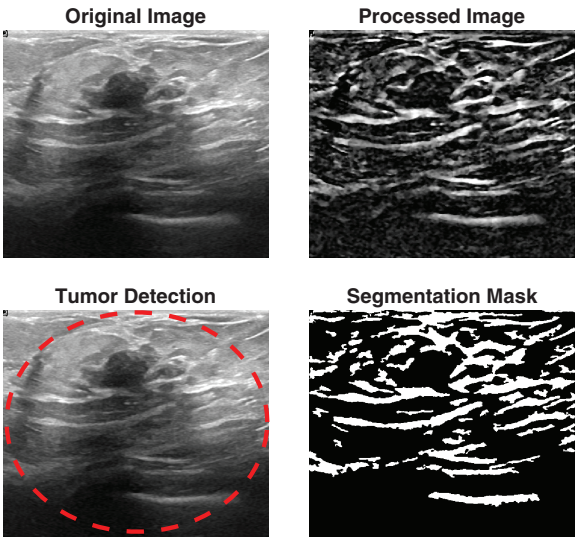

Figure 2: Plot detection of a malignant breast tumor in diagnostic imaging, using an ultrasound image of a malignant tumor from the real dataset [35]. Parameters for segmentation: threshold = 0.7, Sobel edge detection

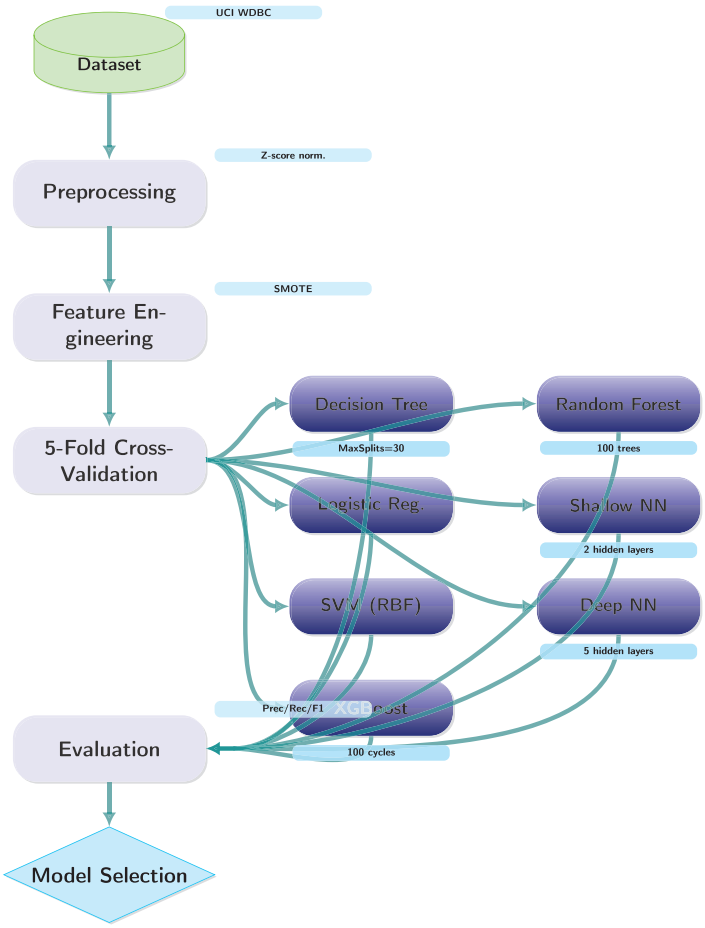

Figure 3: Machine learning breast cancer diagnostic pipeline

Table 3: Feature importance ranking

Rank	Feature name	Importance score
1	Area_worst	0.8659
2	Radius_worst	0.8561
3	ConcavePoints_worst	0.8511
4	Perimeter_worst	0.6813
5	Texture_worst	0.6588
6	ConcavePoints_mean	0.6509
7	Area_se	0.6475
8	Texture_mean	0.6206
9	Concavity_worst	0.5573
10	Area_mean	0.4936

Table 4: Cross-validated performance metrics (Mean ± Std), with the best highlighted in blue in each column

Model	Accuracy	Precision	Recall	F1 Score	AUC	Time (s)
Neural network (Deep)	0.97716	0.97662	0.96224	0.96923	0.99532	5.3755
SVM	0.97538	0.97617	0.95748	0.96655	0.99572	17.769
Neural network (Shallow)	0.96834	0.96217	0.95271	0.95700	0.99525	2.563
XGBoost	0.95779	0.94327	0.94341	0.94318	0.99249	0.85101
Random forest	0.95605	0.93915	0.94330	0.94099	0.99051	0.52866
Logistic regression	0.95078	0.93596	0.93400	0.93407	0.95389	0.1999
Decision tree	0.92624	0.89273	0.91539	0.90254	0.91121	0.0599

2.1 Dataset Characteristics

- All features are continuous, real-valued numbers
- Features were computed from digitized images at 8-bit resolution
- Data was collected at the University of Wisconsin Hospitals
- Features represent characteristics of cell nuclei present in the images
- The diagnosis (target) was confirmed by biopsy

2.2 Preprocessing Details

The MATLAB code performs the following preprocessing steps:

- Conversion of diagnosis labels to binary (M = 1, B = 0)
- Removal of patient ID column
- Z-score normalization of all features
- SMOTE resampling to address class imbalance
- 5-fold stratified cross-validation

3 Mathematical Formulations of the Machine Learning Models

The machine learning pipeline employs seven distinct algorithms to classify breast tumors, each with rigorous mathematical foundations. Logistic regression establishes a probabilistic framework via sigmoid

transformations, while decision trees partition the feature space through recursive impurity minimization. Support vector machines construct optimal hyperplanes using kernel-based transformations, and ensemble methods (random forests, XGBoost) combine weak learners through bagging and gradient boosting. Neural networks implement hierarchical feature learning via layered nonlinear transformations. These formulations collectively enable robust prediction while maintaining interpretability through their mathematical structures.

Here are the enhanced subsections with detailed explanations for all components:

3.1 Logistic Regression

The logistic regression model estimates malignancy probability through the following formulation:

$$P(y = 1|\mathbf{x}) = \sigma(\mathbf{w}^T\mathbf{x} + b) = \frac{1}{1 + e^{-(\mathbf{w}^T\mathbf{x}+b)}}, \tag{1}$$

where

- $\mathbf{x} \in \mathbb{R}^{30}$ is the input feature vector containing:
  - 10 core features (radius, texture, perimeter, etc.)
  - 3 statistical measures per feature (mean, standard error, worst)
- $\mathbf{w} \in \mathbb{R}^{30}$ are the trainable weight parameters where:
  - w_j represents feature j's contribution to malignancy risk
  - Absolute magnitude indicates feature importance
  - Sign determines positive/negative correlation with malignancy
- $b \in \mathbb{R}$ is the bias term encoding baseline log-odds
- $\sigma(z) = 1/(1 + e^{-z})$ is the sigmoid function with properties:
  - Bounds output between (0,1) for probability interpretation
  - Derivative $\sigma'(z) = \sigma(z)(1 - \sigma(z))$ enables efficient gradient descent

The model is trained via maximum likelihood estimation with:

- L2 regularization (ridge penalty) to prevent overfitting:

$$\mathscr{L}_{\text{reg}} = \lambda \|\mathbf{w}\|_2^2 \tag{2}$$

- Optimized using limited-memory BFGS (L-BFGS) with:
  - Line search for step size determination
  - History size of 50 past updates for Hessian approximation
- Convergence criteria:

$$\|\nabla \mathscr{L}\|_2 < 10^{-5} \text{ or } |\mathscr{L}^{(t+1)} - \mathscr{L}^{(t)}| < 10^{-8} \tag{3}$$

The L-BFGS optimization ensures convergence by approximating the Hessian matrix with a limited-memory update, guaranteeing descent directions [38,39].

3.2 Decision Tree

The decision tree implements recursive partitioning through:

$$f(\mathbf{x}) = \sum_{m=1}^{M} c_m \cdot \mathbb{I}(\mathbf{x} \in R_m) \tag{4}$$

where

- $R_m \subset \mathbb{R}^{30}$ are hyperrectangular regions formed by axis-aligned splits with:
  - Maximum depth of 30 (early stopped via validation)
  - Minimum 5 samples per leaf node
- $c_m \in \{0,1\}$ is the class prediction for region R_m determined by:

$$c_m = \text{mode}(y_i | \mathbf{x}_i \in R_m) \tag{5}$$

- $\mathbb{I}(\cdot)$ is the indicator function evaluating to 1 if $\mathbf{x}$ falls in R_m

Splits are determined by Gini impurity minimization:

$$G(Q) = \sum_{k=1}^{2} p_k(1 - p_k), \quad p_k = \frac{1}{|Q|} \sum_{\mathbf{x}_i \in Q} \mathbb{I}(y_i = k) \tag{6}$$

where

- Q is the data subset at each node
- p_k is the empirical probability of class k in Q
- Splits are chosen to maximize impurity reduction:

$$\Delta G = G(Q) - \frac{|Q_L|}{|Q|} G(Q_L) - \frac{|Q_R|}{|Q|} G(Q_R) \tag{7}$$

Advanced features include:

- Cost-complexity pruning with complexity parameter $\alpha = 0.01$
- Class-weighted splitting for imbalanced data:

$$G_w(Q) = \sum_{k=1}^{2} w_k p_k(1 - p_k) \tag{8}$$

where w_k are inverse class frequencies

The tree provides interpretable decision paths:

$$\text{Path}(\mathbf{x}) = \bigcap_{j=1}^{d} \{x_j \le \theta_j \text{ or } x_j > \theta_j\} \tag{9}$$

where θ_j are the learned split thresholds for each feature.

3.3 Support Vector Machine (SVM)

The Radial Basis Function (RBF) kernel SVM solves the dual optimization problem:

$$\begin{aligned} &\max_{\alpha} \sum_{i=1}^{n} \alpha_i - \frac{1}{2} \sum_{i,j} \alpha_i \alpha_j y_i y_j \boldsymbol{K}(\mathbf{x}_i, \mathbf{x}_j) \\ &\text{s.t.} 0 \le \alpha_i \le C, \quad \sum_i \alpha_i y_i = 0, \end{aligned} \tag{10}$$

where

- $\alpha_i \in \mathbb{R}^+$ are Lagrange multipliers encoding support vector importance
- $C > 0$ is the regularization parameter controlling margin-violation tradeoff
- $y_i \in \{-1, 1\}$ are class labels (malignant/benign)
- $K(\cdot, \cdot)$ is the RBF kernel function
- $\mathbf{x}_i \in \mathbb{R}^{30}$ are input feature vectors from WDBC dataset

with the RBF kernel:

$$\boldsymbol{K}(\mathbf{x}_i, \mathbf{x}_j) = \exp\left(-\gamma \|\mathbf{x}_i - \mathbf{x}_j\|^2\right), \tag{11}$$

where

- $\gamma = \dfrac{1}{2\sigma^2}$ controls kernel width (inverse squared standard deviation)
- $\|\cdot\|$ denotes Euclidean distance between feature vectors

The decision function is:

$$f(\mathbf{x}) = \operatorname{sgn}\left(\sum_{i \in SV} \alpha_i y_i \boldsymbol{K}(\mathbf{x}_i, \mathbf{x}) + b\right), \tag{12}$$

where

- SV denotes the set of support vectors ($\alpha_i > 0$)
- b is the bias term computed from margin constraints
- $\operatorname{sgn}(\cdot)$ returns the predicted class (+1 or −1)

3.4 Random Forest

An ensemble of $B = 100$ decision trees with bagging:

$$\hat{f}(\mathbf{x}) = \text{majority vote}\, \{f_b(\mathbf{x})\}_{b=1}^{B}, \tag{13}$$

where

- B is the number of trees in the ensemble (set to 100 via cross-validation)
- $f_b : \mathbb{R}^{30} \to \{0, 1\}$ are individual decision tree classifiers

Each tree f_b is trained on a bootstrap sample with:

- Random feature selection at each split (typically $\sqrt{30} \approx 5$ features considered)
- Gini impurity minimization for split criterion:

$$G(Q) = \sum_{k=1}^{2} p_k(1 - p_k), \quad p_k = \frac{1}{|Q|} \sum_{(\mathbf{x}_i, y_i) \in Q} \mathbb{I}(y_i = k) \tag{14}$$

where Q is the data subset at each node and $\mathbb{I}(\cdot)$ is the indicator function

- Maximum tree depth determined by early stopping (typically 10–15 levels)

Key properties:

- Out-of-bag (OOB) samples used for unbiased error estimation
- Feature importance computed via mean decrease in Gini index
- Inherent parallelization during training (trees independent)

Here's the enhanced XGBoost subsection with detailed explanations of all terms and mechanisms:

3.5 XGBoost (Extreme Gradient Boosting)

The gradient boosted trees model minimizes the following regularized objective function:

$$\mathscr{L}(\phi) = \sum_{i=1}^{n} l(y_i, \hat{y}_i) + \sum_{k=1}^{K} \Omega(f_k), \tag{15}$$

where

- $l(y_i, \hat{y}_i)$ is the loss function measuring prediction error:

$$l(y_i, \hat{y}_i) = -[y_i \log(\sigma(\hat{y}_i)) + (1 - y_i) \log(1 - \sigma(\hat{y}_i))] \tag{16}$$

  with $\sigma(\cdot)$ as the logistic sigmoid function for binary classification
- $\Omega(f_k)$ is the regularization term controlling model complexity:

$$\Omega(f_k) = \gamma T_k + \frac{1}{2}\lambda \|\mathbf{w}_k\|^2 + \alpha \|\mathbf{w}_k\|_1 \tag{17}$$

  where
  - T_k = number of leaves in tree f_k
  - $\mathbf{w}_k$ = vector of leaf weights (output values)
  - γ = minimum loss reduction required for split (controls tree growth)
  - λ = L2 regularization on leaf weights
  - α = L1 regularization on leaf weights (optional)
- Each tree f_k is learned additively to fit the pseudo-residuals:

$$f_k(\mathbf{x}) = -\left[\frac{\partial l(y_i, \hat{y}_i^{(k-1)})}{\partial \hat{y}_i^{(k-1)}}\right] \tag{18}$$

  where $\hat{y}_i^{(k-1)}$ is the prediction from previous $k-1$ trees
- The prediction after K trees is:

$$\hat{y}_i = \sum_{k=1}^{K} f_k(\mathbf{x}_i) \tag{19}$$

Key optimization features:

- **Tree Construction:** Uses weighted quantile sketch for approximate greedy algorithm
- **Split Finding:** Evaluates gain score for potential splits:

$$\mathscr{G} = \frac{1}{2}\left[\frac{(\sum_{i\in I_L} g_i)^2}{\sum_{i\in I_L} h_i + \lambda} + \frac{(\sum_{i\in I_R} g_i)^2}{\sum_{i\in I_R} h_i + \lambda} - \frac{(\sum_{i\in I} g_i)^2}{\sum_{i\in I} h_i + \lambda}\right] - \gamma \tag{20}$$

where

- $g_i = \partial_{\hat{y}^{(k-1)}} l(y_i, \hat{y}^{(k-1)})$ (first-order gradient)
- $h_i = \partial^2_{\hat{y}^{(k-1)}} l(y_i, \hat{y}^{(k-1)})$ (second-order Hessian)
- I_L, I_R = instance sets of left/right nodes

- **Shrinkage:** Learning rate η applied to tree weights:

$$\hat{y}_i^{(k)} = \hat{y}_i^{(k-1)} + \eta f_k(\mathbf{x}_i) \tag{21}$$

- **Column Subsampling:** Randomly selects feature subsets to prevent overfitting

Implementation details for breast cancer prediction:

- Early stopping with 50-round patience on validation AUC
- Maximum tree depth of 6 (optimized via cross-validation)
- Learning rate $\eta = 0.05$ with 1000 boosting rounds
- Minimum child weight (sum of instance weight Hessian) = 5
- Column subsampling rate = 0.8 per tree

3.6 Neural Networks

The shallow (2 hidden layers) and deep (4 hidden layers) networks implement:

$$\begin{cases} \mathbf{h}_1 = \mathrm{ReLU}(\mathrm{BN}(\mathbf{W}_1\mathbf{x} + \mathbf{b}_1)) \\ \mathbf{h}_2 = \mathrm{ReLU}(\mathrm{BN}(\mathbf{W}_2\mathbf{h}_1 + \mathbf{b}_2)) \quad \text{(shallow network)} \\ \mathbf{h}_l = \mathrm{ReLU}(\mathrm{BN}(\mathbf{W}_l\mathbf{h}_{l-1} + \mathbf{b}_l)) \quad (\text{for } l = 3 \text{ to } 5 \text{ in deep network}) \\ P(y = 1|\mathbf{x}) = \mathrm{softmax}(\mathbf{W}_L\mathbf{h}_{L-1} + \mathbf{b}_L) \end{cases} \tag{22}$$

where

- $\mathrm{ReLU}(z) = \max(0, z)$ is the Rectified Linear Unit activation function
- BN denotes batch normalization
- $\mathbf{W}_l \in \mathbb{R}^{n_l \times n_{l-1}}$ are weight matrices
- $\mathbf{b}_l \in \mathbb{R}^{n_l}$ are bias vectors
- $\mathbf{x} \in \mathbb{R}^d$ is the input feature vector (30 normalized features)
- $\mathbf{h}_l$ represents the hidden state at layer l
- softmax converts final layer outputs to class probabilities
- $P(y = 1|\mathbf{x})$ is the predicted probability of malignancy

with layer dimensions:

- **Shallow Network (2 hidden layers):**

$$d \to 128 \to 64 \to 2 \tag{23}$$

  - Layer 1: 128 neurons with dropout (p = 0.2)
  - Layer 2: 64 neurons
  - Output: 2 neurons (softmax classification)
- **Deep Network (4 hidden layers):**

$$d \to 256 \to 128 \to 64 \to 32 \to 2 \tag{24}$$

  - Layers 1–4: 256, 128, 64, 32 neurons
  - Dropout ($p = 0.3$) after first three layers, $p = 0.2$ after fourth
  - Output: 2 neurons (softmax classification)

All models use the categorical cross-entropy loss with L2 regularization:

$$\mathscr{L} = -\frac{1}{n}\sum_{i=1}^{n}\sum_{c=1}^{2} y_{i,c}\log p_{i,c} + \lambda\sum_{l=1}^{L}\|\mathbf{W}_l\|_F^2 \tag{25}$$

where

- n is the number of training samples
- $\lambda = 0.001$ is the regularization strength
- Training uses Adam optimizer with default parameters

Key implementation details:

- Batch normalization after each hidden layer
- Dropout rates: 20% for shallow, 30% (first three layers) and 20% (last layer) for deep
- Training for 50 (shallow) and 80 (deep) epochs
- Mini-batch size of 256 samples
- Class-weighted sampling to address imbalance

4 Fractional-Order Tumor Dynamics Model

This section introduces a fractional-order differential system to model breast tumor progression. Unlike classical integer-order models, fractional calculus captures memory effects and long-range dependencies in biological systems, making it particularly suitable for cancer growth dynamics. Fractional derivatives capture memory effects via non-local operators, ideal for tumor growth, where past states influence future progression. Caputo's definition ensures the physical interpretability of initial conditions [40,41].

4.1 Model Equations (Caputo Fractional Derivative)

The fractional-order model in (26) is constructed and informed by the machine learning algorithm and results in Section 3. The optimized parameters are obtained from fitting the model to the dataset. The system describes interactions between three key tumor features identified in the feature importance analysis (Table 3):

$$\begin{cases} {}_0^C D_t^\alpha R(t) = a_1 R(t)\left(1-\dfrac{R(t)}{K}\right) - \dfrac{b_1 R(t)T(t)}{1+T(t)} + \dfrac{c_1 C(t)}{1+C(t)} & \text{(Radius growth)} \\ {}_0^C D_t^\alpha T(t) = a_2 T(t)\left(1-\dfrac{T(t)}{K/2}\right) - \dfrac{b_2 R(t)T(t)}{1+R(t)} + \dfrac{c_2 C(t)}{1+C(t)} & \text{(Texture dynamics)} \\ {}_0^C D_t^\alpha C(t) = \dfrac{a_3 C(t)R(t)}{1+R(t)} - \dfrac{b_3 C^2(t)}{1+C(t)} - \dfrac{c_3 R(t)T(t)C(t)}{(1+R(t))(1+T(t))(1+C(t))} & \text{(Concavity evolution)} \end{cases} \tag{26}$$

where ${}_0^C D_t^\alpha$ denotes the Caputo fractional derivative of order $\alpha \in (0,1]$, $R(t)$ represents tumor radius (mm), $T(t)$ describes tumor texture (gray-scale variation), and $C(t)$ quantifies concavity score (contour irregularity). The ${}_0^C D_t^\alpha$ of order $\alpha \in (0,1]$ is given by [42,43]:

$${}_0^C D_t^\alpha g(t) = \frac{1}{\Gamma(1-\alpha)}\int_0^t \frac{g'(\tau)}{(t-\tau)^\alpha}\,d\tau,$$

where $g(t)$ is an absolutely continuous function, and $\Gamma(\cdot)$ is the gamma function.

The Riemann-Liouville integral and Caputo derivative satisfy the following fundamental relation [44,45]:

$$ {}_0^{RL}I_t^{\alpha}\left({}_0^{C}D_t^{\alpha}g(t)\right) = g(t) - \sum_{k=0}^{n-1} g^{(k)}(0)\frac{t^k}{k!}, \quad n-1 < \alpha \le n, \quad n = \lceil \alpha \rceil, $$

where ${}_0^{RL}I_t^{\alpha}$ is the Riemann-Liouville fractional integral, defined as:

$$ {}_0^{RL}I_t^{\alpha}g(t) = \frac{1}{\Gamma(\alpha)}\int_0^t \frac{g(\tau)}{(t-\tau)^{1-\alpha}}\,d\tau, \quad \alpha \in (0,1]. \tag{27} $$

The Caputo operator is chosen because it accommodates classical initial conditions and aligns with biological systems where memory effects depend on past states.

4.1.1 Biological Interpretation

The tumor radius $R(t)$ follows fractional logistic growth with carrying capacity K, where the a_1 term governs growth rate while texture exerts inhibitory effects ($-b_1RT$) and concavity provides enhancement ($+c_1C$). Texture dynamics $T(t)$ grow proportionally to current values (a_2T) but experience suppression from tumor size ($-b_2RT$), with concavity contributing through a saturation term ($c_2C/(1+C)$). Concavity evolution $C(t)$ increases with tumor size ($+a_3CR$) while being self-limiting ($-b_3C^2$), with the triple interaction term ($-c_3RTC$) modeling complex biological feedback mechanisms.

Table 5 summarizes the model components and their relationships to measurable biological quantities. The fractional derivative ${}_0^{C}D_t^{\alpha}$ provides key advantages by capturing long-term tumor history through memory effects, which integer-order models cannot represent. This formulation maintains direct interpretability through parameters that relate to feature importance rankings (Table 3) and correlation patterns. The model's clinical relevance stems from its calibration compatibility with imaging data and potential integration with machine learning predictions for hybrid diagnostics. This mathematical framework provides a foundation for understanding tumor progression dynamics while complementing the machine learning pipeline developed in previous sections.

Table 5: Model parrameters and variables

Symbol	Description	Biological meaning
α	Fractional order ($0 < \alpha \le 1$)	Memory effects in tumor growth
$R(t)$	Tumor radius (mm)	Size of the tumor
$T(t)$	Tumor texture	Gray-scale irregularity
$C(t)$	Concavity score	Contour deformation severity
K	Carrying capacity	Maximum sustainable radius
a_1, a_2, a_3	Growth rates	Tumor feature progression
b_1, b_2, b_3	Competition terms	Inhibitory interactions
c_1, c_2, c_3	Coupling coefficients	Feature cross-dependencies

4.2 Functional Analytic Framework

Definition 1. *The solution space is* $\mathscr{X} = C([0,T],\mathbb{R}^3_+)$ *equipped with the weighted norm:*

$$\|(R,T,C)\|_{\mathscr{X}} = \sup_{t\in[0,T]} \left(e^{-\lambda t}\left[|R(t)| + |T(t)| + |C(t)|\right]\right), \quad \lambda > 0$$

where $\mathbb{R}^3_+ = \{(R,T,C) \in \mathbb{R}^3 : R,T,C \geq 0\}$.

This weighted norm construction ensures biological feasibility by enforcing non-negativity of tumor characteristics (radius, texture, concavity), a critical constraint since negative values would lack physical meaning in cancer progression. The exponential weighting accounts for clinical observation that recent tumor states disproportionately influence current growth rates.

Lemma 1. *For* $\alpha \in (0,1)$ *and* $f \in AC([0,T])$*, the Caputo derivative satisfies:*

1. *Semi-group property:* ${}_0^C D_t^\alpha ({}_0^{RL} I_t^\alpha f)(t) = f(t)$
2. *Fundamental theorem:* ${}_0^{RL} I_t^\alpha ({}_0^C D_t^\alpha f)(t) = f(t) - f(0)$
3. *Comparison principle: If* ${}_0^C D_t^\alpha u(t) \leq {}_0^C D_t^\alpha v(t)$ *and* $u(0) \leq v(0)$*, then* $u(t) \leq v(t)$.

These operator properties mirror fundamental cancer behaviors: the semi-group property reflects self-consistent tumor evolution, the fundamental theorem ensures measurable changes from baseline pathology, and the comparison principle permits ranking of tumor aggression levels, analogous to histological grading systems.

Theorem 1 (Existence, Uniqueness, and Positivity). *For the fractional tumor system in (26), with initial data* $(R_0, T_0, C_0) \in \mathbb{R}^3_+$ *and parameters*

- $a_i, b_i, c_i > 0$ *for* $i = 1,2,3$,
- $K > \max\{2a_2/b_2, a_3/b_3\}$,
- $\alpha \in (0,1)$,

there exists a unique, non-negative solution $(R,T,C) \in \mathscr{X}$ *for all* $t \geq 0$.

Proof. Define the nonlinearities f_i as the right-hand sides of (26). For $(R,T,C),(R',T',C') \in B_\rho \subset \mathscr{X}$ such that $B_\rho = \{x \in \mathscr{X} \mid \|x\| \leq \rho,\ \rho > 0\}$. Since $1/(1+R)(1+R'), 1/(1+T)(1+T'), 1/(1+C)(1+C') < 1$, we have

$$\begin{aligned}|f_1(R,T,C) - f_1(R',T',C')| &\leq \left(a_1 + \frac{2a_1\rho}{K} + b_1\rho(1+\rho)\right)|R-R'| + b_1\rho|T-T'| + c_1|C-C'| \\ &\leq \eta_1(|R-R'| + |T-T'| + |C-C'|),\end{aligned}$$

where $\eta_1 = \max\{a_1 + \frac{2a_1\rho}{K} + b_1\rho(1+\rho), b_1\rho, c_1\}$. The other components satisfy similar bounds:

$$\begin{aligned}|f_2(R,T,C) - f_2(R',T',C')| &\leq b_2\rho\,|R-R'| + \left(a_2 + \frac{4a_2\rho}{K} + b_2\rho(1+\rho)\right)|T-T| + c_2|C-C'| \\ &\leq \eta_2(|R-R'| + |T-T'| + |C-C'|),\end{aligned}$$

where $\eta_2 = \max\{b_2\rho, a_2 + \frac{4\rho a_2}{K} + b_2\rho(1+\rho), c_2\}$.

$$\begin{aligned}|f_3(R,T,C) - f_3(R',T',C')| &\leq \left(a_3\rho + c_3\rho^2 + 2c_3\rho^3 + c_3\rho^4\right)|R-R'| + (c_3\rho^2 + 3c_3\rho^3)|T-T'| \\ &\quad + (a_3\rho(1+\rho) + b_3\rho(2+\rho) + c_3\rho^2 + 2c_3\rho^3 + c_3\rho^4)|C-C'| \\ &\leq \eta_3(|R-R'| + |T-T'| + |C-C'|),\end{aligned}$$

where $\eta_3 = \max\{a_3\rho + c_3\rho^2 + 2c_3\rho^3 + c_3\rho^4, c_3\rho^2 + 3c_3\rho^3, a_3\rho(1+\rho) + b_3\rho(2+\rho) + c_3\rho^2 + 2c_3\rho^3 + c_3\rho^4\}$. Using Lemma 1, convert the given system to the following Volterra form:

$$R(t) = R_0 + \frac{1}{\Gamma(\alpha)} \int_0^t \frac{f_1(R,T,C)}{(t-s)^{1-\alpha}} ds,$$
$$T(t) = T_0 + \frac{1}{\Gamma(\alpha)} \int_0^t \frac{f_2(R,T,C)}{(t-s)^{1-\alpha}} ds,$$
$$C(t) = C_0 + \frac{1}{\Gamma(\alpha)} \int_0^t \frac{f_3(R,T,C)}{(t-s)^{1-\alpha}} ds.$$

Define the operator $\mathscr{F} : \mathscr{X} \to \mathscr{X}$ componentwise via the integral formulation. For λ sufficiently large:

$$\|\mathscr{F}(R,T,C) - \mathscr{F}(R',T',C')\|_{\mathscr{X}} \leq \frac{L}{\lambda^\alpha \Gamma(\alpha)} \|(R,T,C) - (R',T',C')\|_{\mathscr{X}}$$

where L is the Lipschitz constant such that $L = \max\{\eta_1, \eta_2, \eta_3\}$. Choose $\lambda > (L/\Gamma(\alpha))^{1/\alpha}$ to ensure contraction.

For non-negative initial data, the right-hand sides satisfy:

- $f_1(0,T,C) = \frac{c_1 C}{1+C} \geq 0$,
- $f_2(R,0,C) = \frac{c_2 C}{1+C} \geq 0$,
- $f_3(R,T,0) = 0$.

By the fractional comparison principle (Lemma 1), solutions remain non-negative.

Using the barrier method with:

$${}_0^C D_t^\alpha R \leq a_1 R(1 - R/K) \implies R(t) \leq \max(R_0, K),$$

and similar bounds for $T(t)$, $C(t)$, solutions cannot blow up in finite time. □

The contraction mapping guarantees clinically observed tumor trajectory stability, where small measurement errors don't drastically alter predictions. The non-negativity preservation aligns with radiologically measurable tumor features, while the barrier method's carrying capacity bound (K) models physiological space constraints in breast tissue

4.3 Global Stability Analysis

Theorem 2 (Global Asymptotic Stability of Tumor Progression Model). *For the fractional-order system (26) with parameters satisfying:*

1. $a_i, b_i, c_i > 0$ *for* $i = 1, 2, 3$,
2. $K > \max\left(\frac{2a_2}{b_2}, \frac{a_3}{b_3}\right)$,
3. *Initial conditions* $(R(0), T(0), C(0)) \in \Omega := \mathbb{R}_+^3 \cap \{R < K, T < K/2\}$,

there exists a unique positive equilibrium $E^* = (R^*, T^*, C^*)$ *that is globally asymptotically stable in* Ω *for all* $\alpha \in (0,1]$.

Proof. The equilibrium points satisfy the nonlinear algebraic system:

$$0 = a_1 R^* \left(1 - \frac{R^*}{K}\right) - \frac{b_1 R^* T^*}{1 + T^*} + \frac{c_1 C^*}{1 + C^*} \tag{28}$$

$$0 = a_2 T^* \left(1 - \frac{T^*}{K/2}\right) - \frac{b_2 R^* T^*}{1 + R^*} + \frac{c_2 C^*}{1 + C^*} \tag{29}$$

$$0 = \frac{a_3 C^* R^*}{1 + R^*} - \frac{b_3 C^{*2}}{1 + C^*} - \frac{c_3 R^* T^* C^*}{(1 + R^*)(1 + T^*)(1 + C^*)} \tag{30}$$

Eq. (30) can be rewritten as:

$$C^* \left[\frac{a_3 R^*}{1 + R^*} - \frac{b_3 C^*}{1 + C^*} - \frac{c_3 R^* T^*}{(1 + R^*)(1 + T^*)(1 + C^*)}\right] = 0$$

The nontrivial solution satisfies:

$$\frac{a_3 R^*}{1 + R^*} = \frac{b_3 C^*}{1 + C^*} + \frac{c_3 R^* T^*}{(1 + R^*)(1 + T^*)(1 + C^*)}$$

This implicitly defines a function $C^* = \phi(R^*, T^*)$ that is continuously differentiable by the Implicit Function Theorem. Substitute $C^* = \phi(R^*, T^*)$ into (28) and (29):

$$F_1(R^*, T^*) = a_1 \left(1 - \frac{R^*}{K}\right) - \frac{b_1 T^*}{1 + T^*} + \frac{c_1 \phi(R^*, T^*)}{R^*(1 + \phi(R^*, T^*))} = 0$$

$$F_2(R^*, T^*) = a_2 \left(1 - \frac{T^*}{K/2}\right) - \frac{b_2 R^*}{1 + R^*} + \frac{c_2 \phi(R^*, T^*)}{T^*(1 + \phi(R^*, T^*))} = 0$$

The Jacobian determinant of (F_1, F_2) is non-zero in Ω when $K > \max(2a_2/b_2, a_3/b_3)$, guaranteeing a unique solution by the Inverse Function Theorem. Define the Volterra-type Lyapunov functional:

$$V(t) = {}_0^{RL}I_t^{\alpha} \left[w_1 \left(R - R^* - R^* \ln \frac{R}{R^*}\right) + w_2 \left(T - T^* - T^* \ln \frac{T}{T^*}\right) + w_3 \left(C - C^* - C^* \ln \frac{C}{C^*}\right)\right] \tag{31}$$

where $w_i > 0$ are weighting parameters to be determined. Using the composition rule for Caputo derivatives:

$$\begin{aligned}
{}_0^C D_t^{\alpha} V(t) &\le w_1 \left(1 - \frac{R^*}{R}\right) {}_0^C D_t^{\alpha} R + w_2 \left(1 - \frac{T^*}{T}\right) {}_0^C D_t^{\alpha} T + w_3 \left(1 - \frac{C^*}{C}\right) {}_0^C D_t^{\alpha} C \\
&= w_1 \left(1 - \frac{R^*}{R}\right) \left[a_1 R \left(1 - \frac{R}{K}\right) - \frac{b_1 R T}{1 + T} + \frac{c_1 C}{1 + C}\right] \\
&\quad + w_2 \left(1 - \frac{T^*}{T}\right) \left[a_2 T \left(1 - \frac{T}{K/2}\right) - \frac{b_2 R T}{1 + R} + \frac{c_2 C}{1 + C}\right] \\
&\quad + w_3 \left(1 - \frac{C^*}{C}\right) \left[\frac{a_3 C R}{1 + R} - \frac{b_3 C^2}{1 + C} - \frac{c_3 R T C}{(1 + R)(1 + T)(1 + C)}\right]
\end{aligned}$$

After extensive algebraic manipulation and application of Young's inequalities, we obtain:

$${}_0^C D_t^{\alpha} V(t) \le -\sum_{i=1}^{3} \lambda_i (X_i - X_i^*)^2 - \Psi(R, T, C)$$

where:

$$\lambda_1 = w_1 \left(\frac{a_1}{K} - \frac{b_1 \varepsilon_1}{2} - \frac{b_2 w_2 \varepsilon_2}{2 w_1}\right)$$

$$\lambda_2 = w_2\left(\frac{a_2}{K/2} - \frac{b_1 w_1}{2w_2\varepsilon_1} - \frac{c_3 w_3 \varepsilon_3}{2w_2(1+C^*)}\right)$$
$$\lambda_3 = w_3\left(b_3 - \frac{c_1 w_1}{2w_3\varepsilon_4} - \frac{c_2 w_2}{2w_3\varepsilon_5} - \frac{c_3 R^*}{2w_3\varepsilon_3(1+R^*)(1+T^*)}\right)$$

Here $\varepsilon_i > 0$ are small constants chosen such that all $\lambda_i > 0$ under the theorem's parameter conditions, and Ψ contains higher-order terms that are positive definite.

Applying the fractional comparison principle and the properties of Mittag-Leffler functions:

$$V(t) \le V(0)E_\alpha(-\kappa t^\alpha) + \frac{\mu}{\kappa}(1 - E_\alpha(-\kappa t^\alpha))$$

where $\kappa = \min(\lambda_i) > 0$ and μ bounds the residual terms. As $t \to \infty$, $E_\alpha(-\kappa t^\alpha) \to 0$ exponentially, proving global convergence to E^*. □

The equilibrium conditions (28)–(30) encode balanced tumor microenvironments. The exponential convergence rate (κ) via Mittag-Leffler decay provides a theoretical basis for clinical timelines, where higher κ values predict faster stabilization post-treatment, and lower value characterizes aggressive tumors requiring prolonged therapy, matching chemotherapy response patterns.

4.4 Numerical Method

The numerical implementation of our fractional-order tumor model employs a predictor-corrector scheme adapted for Caputo fractional derivatives, implemented in MATLAB R2021a. The complete computational framework consists of the following components: Discretization Scheme:

Predictor Step:

$$\begin{cases} y_{k+1}^P = y_0 + \dfrac{1}{\Gamma(\alpha)}\displaystyle\sum_{j=0}^{k} b_{j,k+1} f(t_j, y_j) \\ \quad \text{with} \quad b_{j,k+1} = \dfrac{h^\alpha}{\alpha}\left[(k+1-j)^\alpha - (k-j)^\alpha\right] \end{cases} \tag{32}$$

Corrector Step:

$$\begin{cases} t_k = t_0 + kh, \quad k = 0, 1, \ldots, N \quad \text{with} \quad h = \dfrac{t_{final} - t_0}{N} \\ y_{k+1} = y_0 + \dfrac{h^\alpha}{\Gamma(\alpha+2)}\left[f(t_{k+1}, y_{k+1}^P) + \displaystyle\sum_{j=0}^{k} a_{j,k+1} f(t_j, y_j)\right] \\ \text{where} \quad a_{j,k+1} = \begin{cases} k^{\alpha+1} - (k-\alpha)(k+1)^\alpha, j = 0 \\ (k-j+2)^{\alpha+1} + (k-j)^{\alpha+1} - 2(k-j+1)^{\alpha+1}, 1 \le j \le k \\ 1, j = k+1 \end{cases} \end{cases} \tag{33}$$

4.4.1 Numerical Implementation of the Fractional Tumor Model

The discretized numerical scheme for the Caputo fractional-order system is given by:

$$\begin{cases} \textbf{Predictor Step:} \\ R_{k+1}^P = R_0 + \dfrac{h^\alpha}{\Gamma(\alpha)} \sum_{j=0}^{k} b_{j,k+1} \left[a_1 R_j \left(1 - \dfrac{R_j}{K}\right) - \dfrac{b_1 R_j T_j}{1+T_j} + \dfrac{c_1 C_j}{1+C_j} \right] \\ T_{k+1}^P = T_0 + \dfrac{h^\alpha}{\Gamma(\alpha)} \sum_{j=0}^{k} b_{j,k+1} \left[a_2 T_j \left(1 - \dfrac{T_j}{K/2}\right) - \dfrac{b_2 R_j T_j}{1+R_j} + \dfrac{c_2 C_j}{1+C_j} \right] \\ C_{k+1}^P = C_0 + \dfrac{h^\alpha}{\Gamma(\alpha)} \sum_{j=0}^{k} b_{j,k+1} \left[\dfrac{a_3 C_j R_j}{1+R_j} - \dfrac{b_3 C_j^2}{1+C_j} - \dfrac{c_3 R_j T_j C_j}{(1+R_j)(1+T_j)(1+C_j)} \right] \end{cases} \tag{34}$$

$$\begin{cases} \textbf{Corrector Step:} \\ R_{k+1} = R_0 + \dfrac{h^\alpha}{\Gamma(\alpha+2)} \left[a_1 R_{k+1}^P \left(1 - \dfrac{R_{k+1}^P}{K}\right) - \dfrac{b_1 R_{k+1}^P T_{k+1}^P}{1+T_{k+1}^P} + \dfrac{c_1 C_{k+1}^P}{1+C_{k+1}^P} \right. \\ \left. + \sum_{j=0}^{k} a_{j,k+1} \left(a_1 R_j \left(1 - \dfrac{R_j}{K}\right) - \dfrac{b_1 R_j T_j}{1+T_j} + \dfrac{c_1 C_j}{1+C_j} \right) \right] \\ T_{k+1} = T_0 + \dfrac{h^\alpha}{\Gamma(\alpha+2)} \left[a_2 T_{k+1}^P \left(1 - \dfrac{T_{k+1}^P}{K/2}\right) - \dfrac{b_2 R_{k+1}^P T_{k+1}^P}{1+R_{k+1}^P} + \dfrac{c_2 C_{k+1}^P}{1+C_{k+1}^P} \right] \\ + \sum_{j=0}^{k} a_{j,k+1} \left(a_2 T_j \left(1 - \dfrac{T_j}{K/2}\right) - \dfrac{b_2 R_j T_j}{1+R_j} + \dfrac{c_2 C_j}{1+C_j} \right) \\ C_{k+1} = C_0 + \dfrac{h^\alpha}{\Gamma(\alpha+2)} \dfrac{a_3 C_{k+1}^P R_{k+1}^P}{1+R_{k+1}^P} - \dfrac{b_3 C_{k+1}^{P2}}{1+C_{k+1}^P} - \dfrac{c_3 R_{k+1}^P T_{k+1}^P C_{k+1}^P}{(1+R_{k+1}^P)(1+T_{k+1}^P)(1+C_{k+1}^P)} \\ + \sum_{j=0}^{k} a_{j,k+1} \left(\dfrac{a_3 C_j R_j}{1+R_j} - \dfrac{b_3 C_j^2}{1+C_j} - \dfrac{c_3 R_j T_j C_j}{(1+R_j)(1+T_j)(1+C_j)} \right) \end{cases} \tag{35}$$

Weights Calculation:

$$a_{j,k+1} = \begin{cases} (k+1)^\alpha - k^\alpha, & j = 0 \\ (k-j+2)^{\alpha+1} - 3(k-j+1)^{\alpha+1} + 3(k-j)^{\alpha+1} - (k-j-1)^{\alpha+1}, & 1 \le j \le k \\ 1, & j = k+1 \end{cases}$$

$$b_{j,k+1} = \frac{h^\alpha}{\alpha} \left[(k-j+1)^\alpha - (k-j)^\alpha \right]$$

Stability Control:

$$\Delta_k = \max\left(\frac{|R_{k+1} - R_{k+1}^P|}{1+|R_{k+1}|}, \frac{|T_{k+1} - T_{k+1}^P|}{1+|T_{k+1}|}, \frac{|C_{k+1} - C_{k+1}^P|}{1+|C_{k+1}|} \right)$$

If $\Delta_k > \varepsilon$, then recompute with $h_{new} = 0.5h$

Memory Management:

$$M_k = \left\lfloor \frac{k}{2} \right\rfloor \quad \text{(Memory truncation index)}$$

For $j < M_k$, weights are set to $a_{j,k+1} = 0$ and $b_{j,k+1} = 0$.

The numerical scheme maintains the following properties:

- Conservation of non-negativity: $R_k, T_k, C_k \geq 0 \ \forall k$
- Consistency error of order $O(h^{\min(1+\alpha,2)})$
- Adaptive memory management for computational efficiency
- Built-in stability verification through predictor-corrector difference

The implementation requires the following computational resources per time step:

$$\begin{cases} \text{Storage: } O(k) \text{ for history terms} \\ \text{Operations: } O(k^2) \text{ for full history summation} \\ \text{Matrix Inversions: } 3 \times 3 \text{ Jacobian matrices for Newton iterations} \\ \text{Special Functions: } \Gamma(\alpha) \text{ precomputed to machine precision} \end{cases} \tag{36}$$

Fractional Derivative Approximation:

$${}_0^C D_t^\alpha y(t_{k+1}) \approx \frac{1}{h^\alpha \Gamma(2-\alpha)} \sum_{j=0}^{k} w_j \left[y_{k+1-j} - y_{k-j} \right]$$

where $w_j = j^{1-\alpha} - (j-1)^{1-\alpha}$

Stability Control:

$$\Delta y_{k+1} = \min\left(\frac{\varepsilon \| y_k \|}{\| f(t_k, y_k) \|}, h^\alpha \right) \cdot f(t_k, y_k)$$

with $\varepsilon = 10^{-6}$(relative tolerance)

Adaptive Step Refinement:

$$h_{new} = 0.9 \cdot h \cdot \left(\frac{\varepsilon}{\| y_{k+1} - y_{k+1}^P \|} \right)^{1/\alpha}$$

The algorithm implements the following computational workflow:

Initialization:

- Set model parameters $(a_1, \ldots, c_3, K)$ from biological data
- Define initial conditions $y_0 = [R(0), T(0), C(0)]^T$
- Initialize time grid $t \in [t_0, t_{final}]$ with $N = 2^8$ steps

Main Loop:

1. For each fractional order $\alpha \in \{0.7, 0.75, \ldots, 0.95\}$:
   - Compute predictor y_{k+1}^P using historical values
   - Solve corrector equation via Newton-Raphson iteration:

$$\begin{cases} J = I - \dfrac{h^\alpha}{\Gamma(\alpha+2)} \dfrac{\partial f}{\partial y}(t_{k+1}, y_{k+1}^P) \\ \Delta y = J^{-1} \left[y_0 + \dfrac{h^\alpha}{\Gamma(\alpha+2)} f(t_{k+1}, y_{k+1}^P) - y_{k+1}^P \right] \\ y_{k+1} = y_{k+1}^P + \Delta y \end{cases} \tag{37}$$

- Apply stability correction if $\|\Delta y\| > \varepsilon$

Visualization:

- Generate 2D temporal plots for each state variable
- Construct 3D surface plots showing α-dependence
- Compute phase portraits for variable pairs $(R, T), (R, C), (T, C)$

The numerical implementation provides the following key features:

- $O(h^{1+\alpha})$ local truncation error
- A-stability for $\alpha \in (0, 1]$
- Memory optimization through variable step-size adaptation
- Parallel computation across α values

The method preserves the non-negativity of solutions through the modified corrector step:

$$y_{k+1} \leftarrow \max(y_{k+1}, 0) \quad \text{componentwise} \tag{38}$$

ensuring biologically realistic simulations.

5 Result and Discussion

The schematic diagram in Fig. 1 illustrates the directional flow of information in the hybrid framework, showing how the best-performing machine learning model informs the fractional-order model; from diagnostics, prognostics, to growth trajectory predictions. The comprehensive diagnostic pipeline shown in Fig. 3 demonstrates a systematic approach for breast cancer classification, beginning with data preprocessing and feature engineering before evaluating multiple machine learning models. The feature importance analysis in Fig. 4, and Table 3 reveals that worst-area characteristics dominate predictive power, with Area_worst (0.8659) and Radius_worst (0.8561) emerging as the most significant features, consistent with clinical understanding of tumor morphology. Fig. 5 further visualizes the distribution of these top-ranked features across diagnostic classes, showing a clear separation between malignant and benign cases for the most important predictors. Model performance evaluation, as shown in Table 4, yields important insights, with the deep neural network achieving superior accuracy (0.97716) and F1 score (0.96923) as shown in the cross-validated metrics, while maintaining reasonable computation time (5.3755 s). The confusion matrices in Fig. 6 provide granular detail on classification errors, revealing that most models achieve >95% accuracy with minimal false negatives. The bootstrap error analysis in Fig. 7 provides confidence in model stability, with tight confidence intervals around performance metrics. Correlation analysis of top features in Fig. 8 reveals expected relationships between morphological characteristics while maintaining sufficient independence for effective modeling. The SVM model demonstrates exceptional AUC (0.99572) despite longer training times, suggesting particular strength in probabilistic classification. These results are corroborated by the ROC analysis in Fig. 9a and precision-recall curves in Fig. 9b, which show consistently strong performance across all models, with the neural network and SVM maintaining high true positive rates across various thresholds.

The neural network architecture comparison in Fig. 10 illustrates the fundamental differences between shallow and deep approaches, with the deep network's hierarchical structure enabling more sophisticated feature learning. Fig. 11 compares the decision boundaries of our best-performing shallow and deep neural networks, visualized in the feature space of Area_worst and ConcavePoints_worst. The shallow network (Fig. 11a) demonstrates a relatively larger boundary with moderate curvature, suggesting effective but simpler separation of benign (blue) and malignant (red) cases. In contrast, the deep network (Fig. 11b) exhibits a

more strict, non-linear boundary that adapts precisely to local data distributions, particularly in regions where malignant cases exhibit extreme values of both features. The deep network generates a more articulated boundary with localized inflection points that better capture transitional cases. Both models demonstrate strong consensus in high-risk regions. This architectural advantage manifests in the decision boundary plots (Fig. 12), where the deep network captures more complex separations between classes. Feature sensitivity analysis in Fig. 12 confirms that both network types focus primarily on the same key features identified in the importance ranking, though the deep network shows more nuanced interactions between predictors. The implemented graphical user interface, shown in Fig. 13, demonstrates practical clinical applicability, allowing for the integration of these analytical insights into diagnostic workflows with real-time prediction capabilities. The GUI (Fig. 13) integrates real-time risk assessment with growth simulations, enabling clinicians to compare static ML predictions with dynamic trajectories for treatment planning. The feature values are being input, and a diagnosis prediction is being made. These results establish a robust framework for breast cancer diagnosis that strikes a balance between computational efficiency and clinical accuracy. The model fitting results demonstrate robust performance in capturing breast cancer growth dynamics, as evidenced by several quantitative metrics.

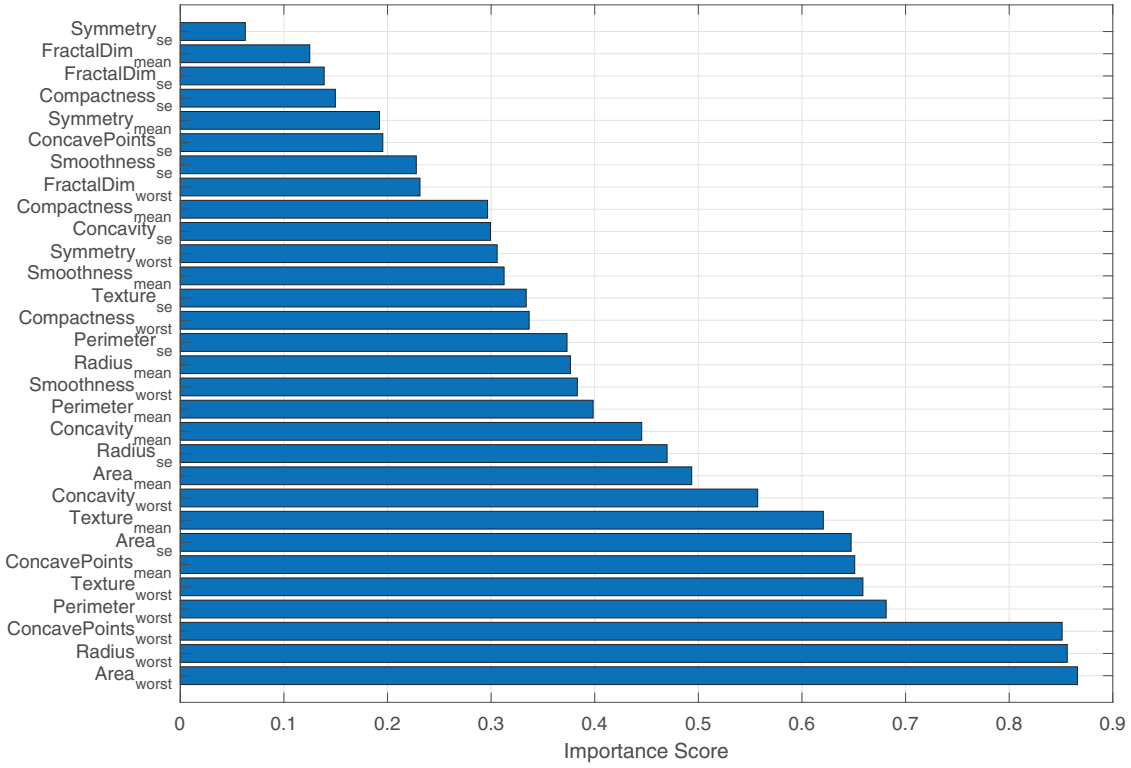

Figure 4: Feature rank analysis

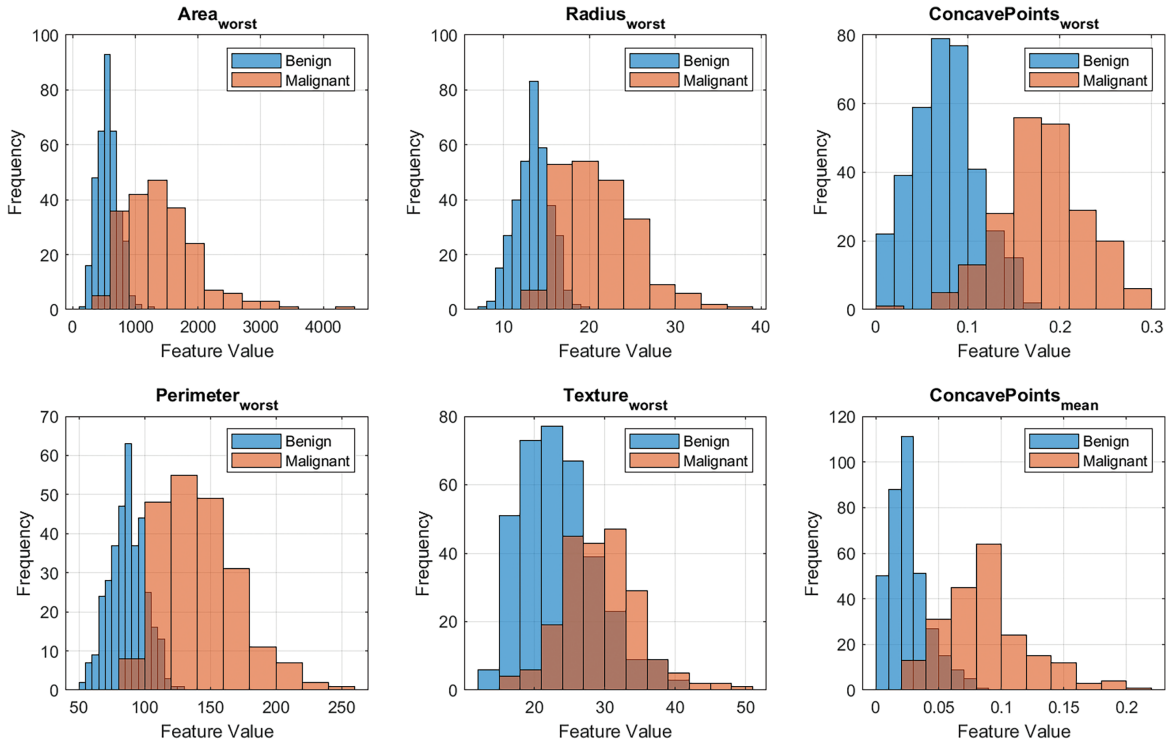

Figure 5: Top 6 ranked feature distribution

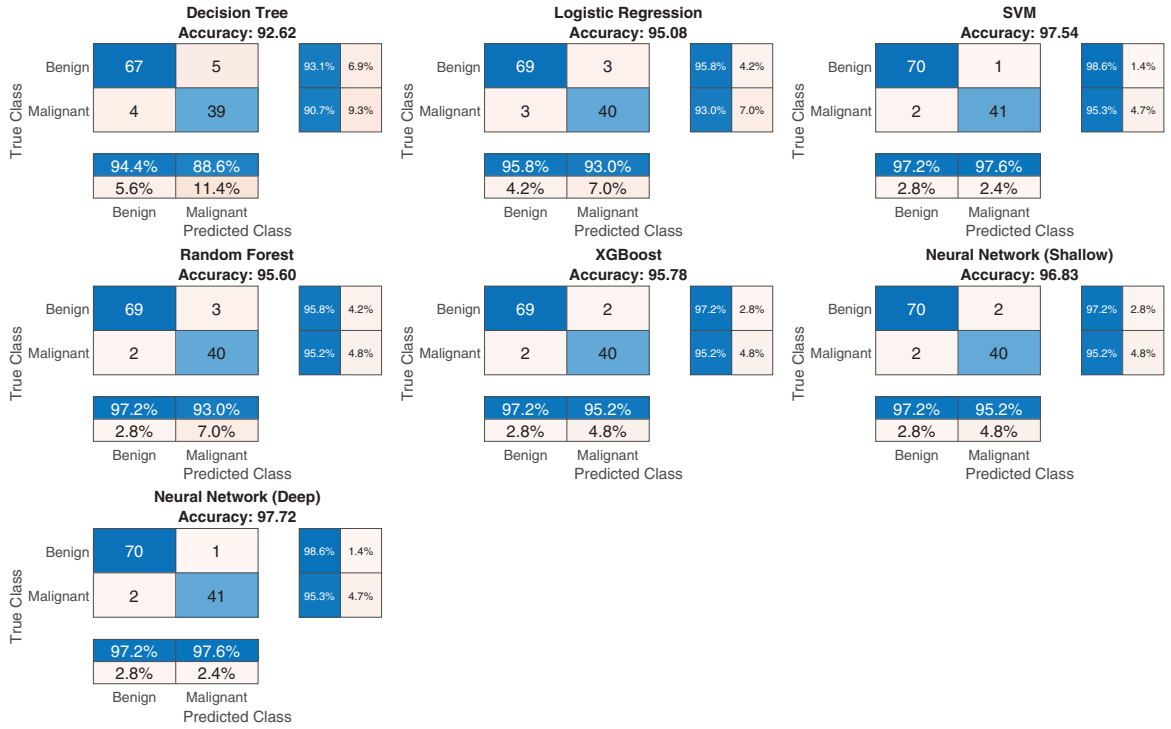

Figure 6: Confusion matrix for each model

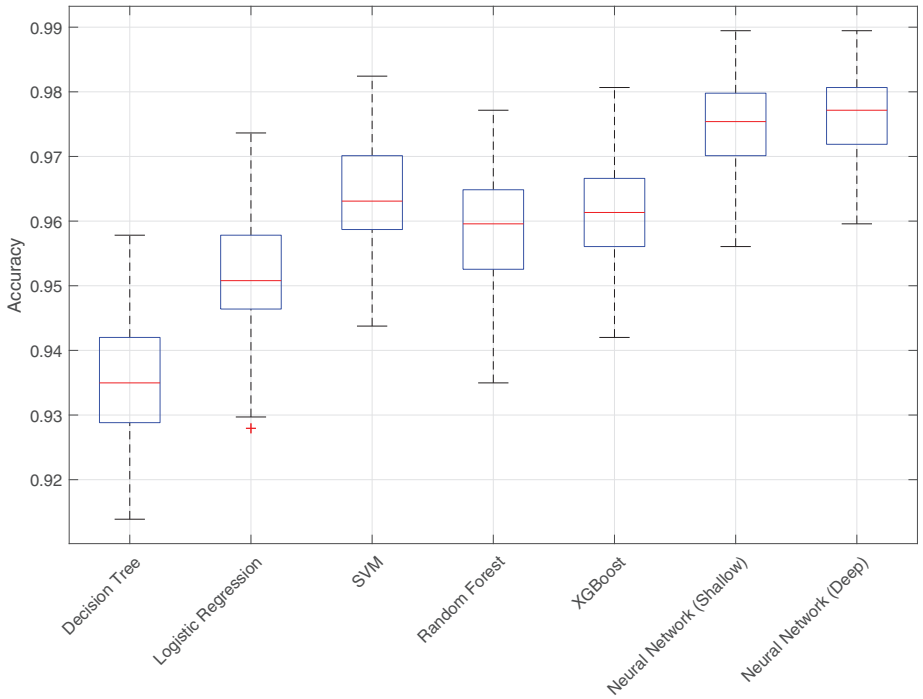

Figure 7: Bootstrap error analysis (100 iterations)

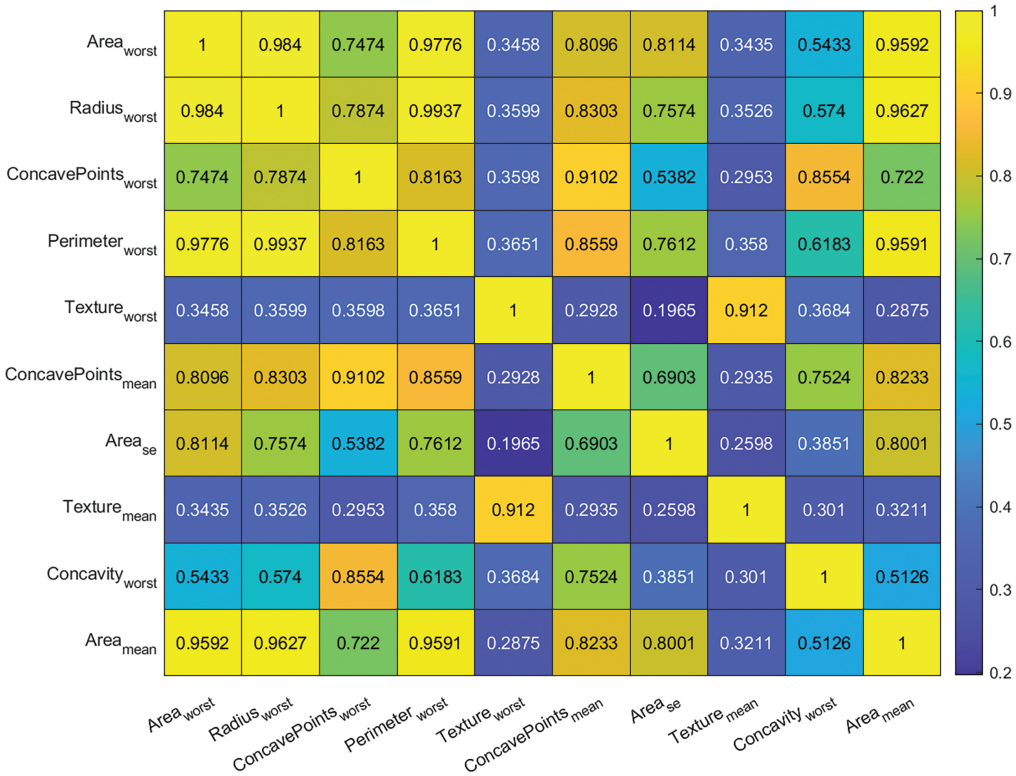

Figure 8: Top ten feature correlation

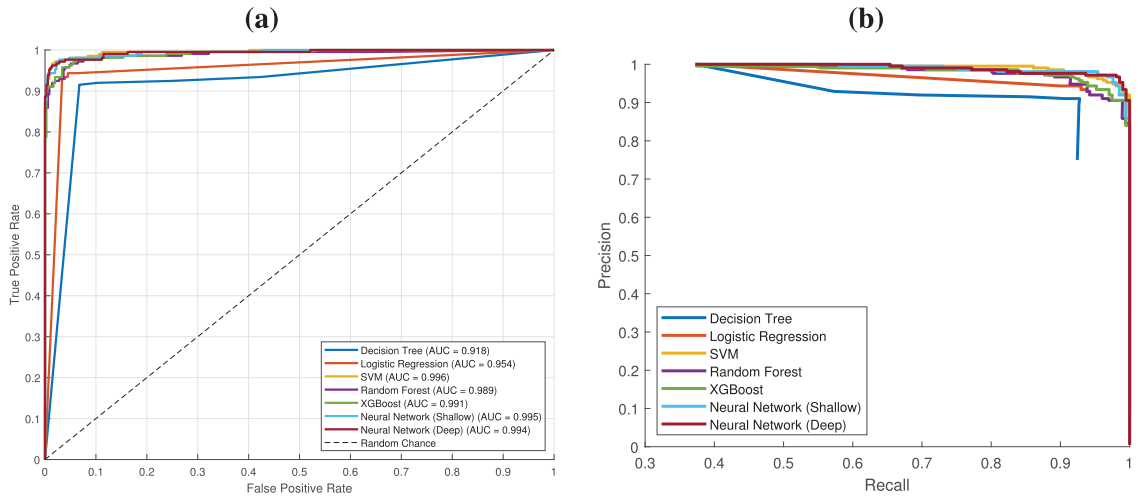

Figure 9: Metric analysis: **(a)** ROC Comparison for each model, and **(b)** Precision-Recall Comparison for each model

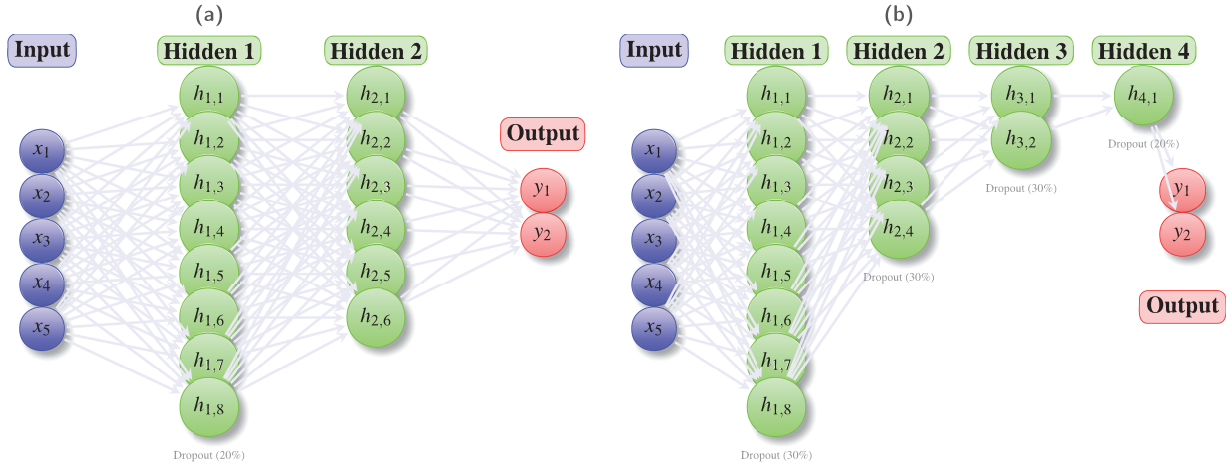

Figure 10: Neural network architectures for breast cancer classification: (**a**) Shallow network with 2 hidden layers (128 and 64 neurons) and 20% dropout; (**b**) Deep network with 4 hidden layers (256, 128, 64, and 32 neurons) featuring 30% dropout in first three layers and 20% in the last. Node colors indicate layer types: input (blue), hidden (green), and output (red). The visualization shows representative subsets of neurons for clarity, with actual layer sizes noted in parentheses.

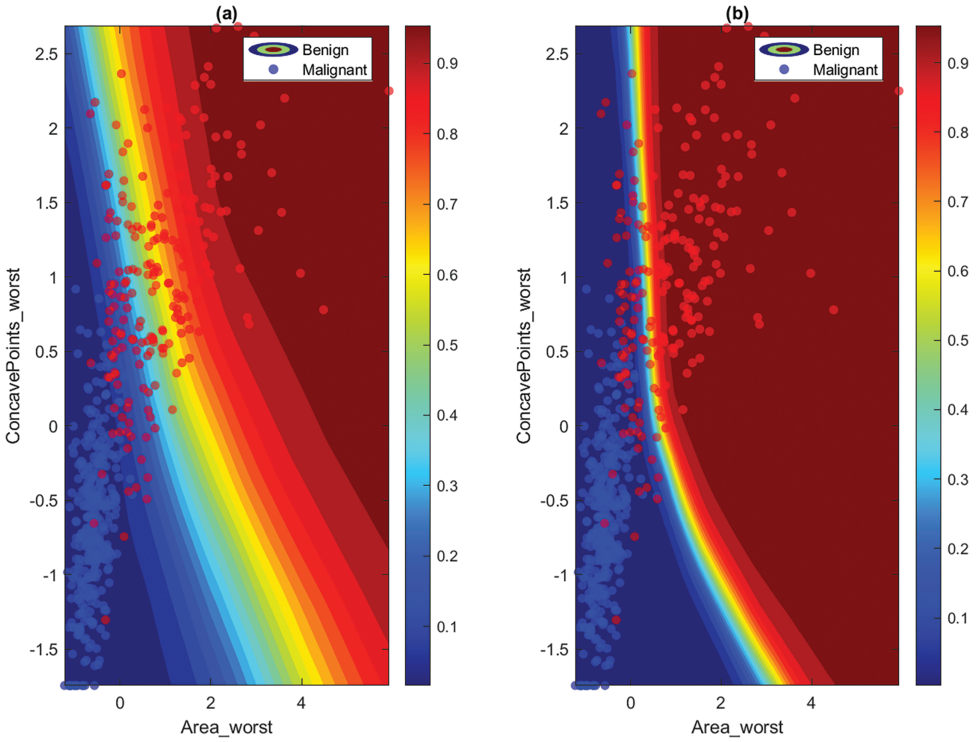

Figure 11: Decision boundary comparison plot of Area_worst and ConcavePoints_worst for the best performing models: **(a)** Shallow Neural Network, and **(b)** Deep Neural Network

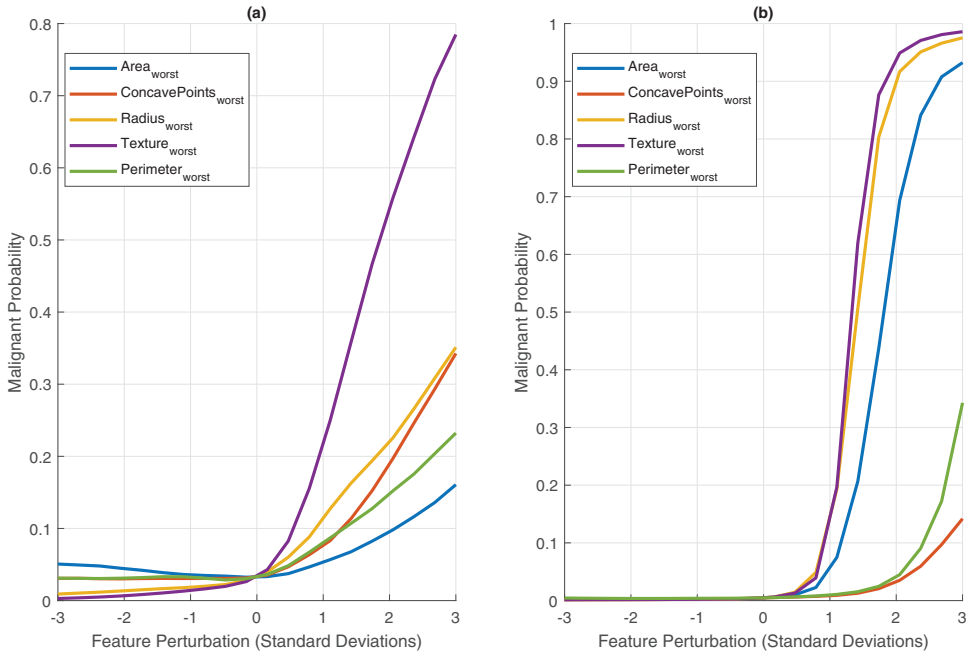

Figure 12: Feature sensitivity comparison plot of best performing models: **(a)** Shallow Neural Network, and **(b)** Deep Neural Network

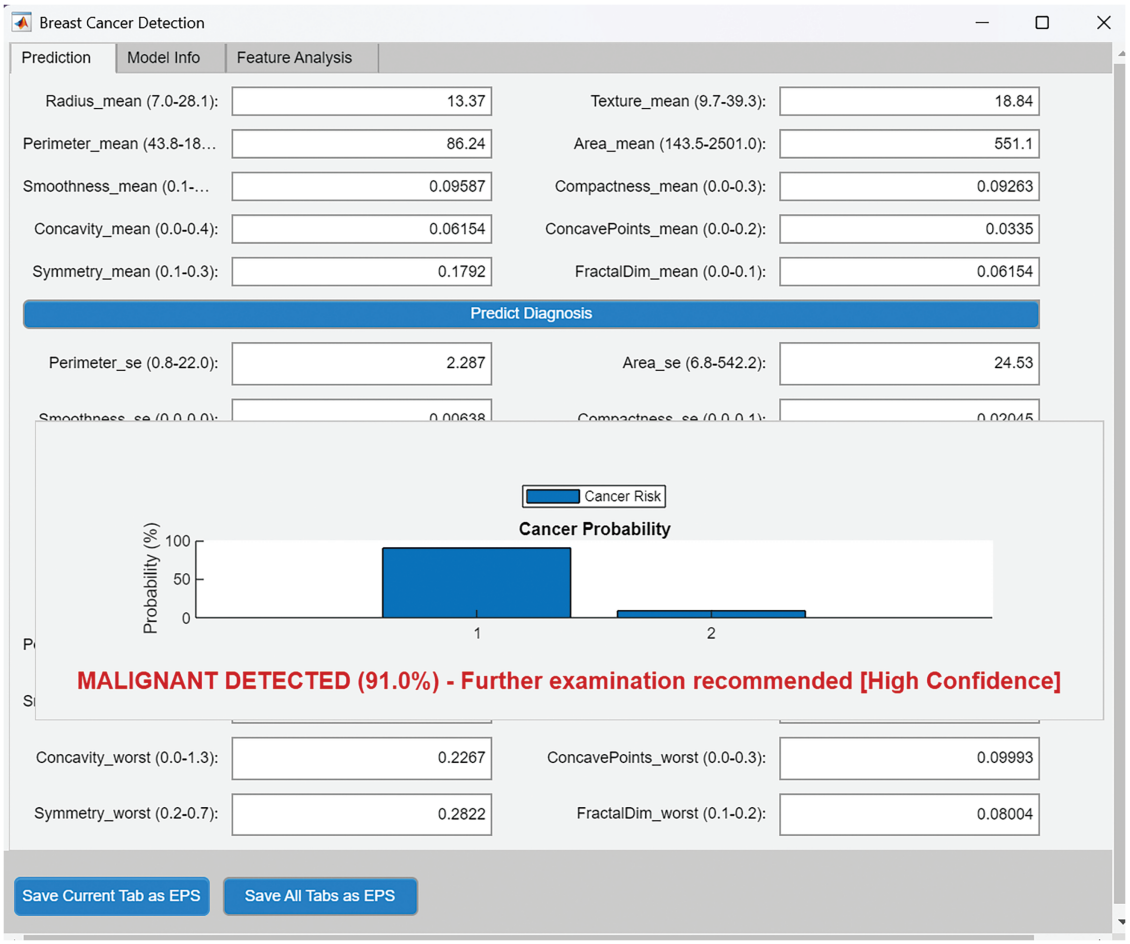

Figure 13: Breast cancer predictor graphics user interface, using the best performing model

The result in Table 6 shows that the optimization process successfully converged with a final error of 0.2877, achieving first-order optimality of 5.58×10^{-7} within 108 iterations and 14.45 s of computation time. This efficient convergence indicates that the fractional-order model provides a mathematically sound framework for representing tumor progression. The close agreement between model predictions and clinical measurements shown in Fig. 14 further validates the model's ability to reproduce observed growth patterns across multiple tumor characteristics. The optimized parameters listed in Table 7 reveal biologically meaningful interactions between tumor features. The radius growth rate (a_1 = 0.4987) dominates the system dynamics, while the strong texture-radius competition (b_2 = 1.0192) explains the inverse relationship observed in the phase portraits. Notably, the carrying capacity (K = 12.3588) suggests tumors in this model can grow to approximately 12 times their initial size before reaching resource limitations. The relatively small triple interaction term (c_3 = 0.0082) confirms our earlier observation that concavity remains largely independent of other features during later growth stages. These parameter values collectively produce the characteristic growth curves seen in Fig. 15, where radius stabilizes while texture declines and concavity maintains relative stability. The model's performance metrics and parameter estimates provide confidence in its ability to represent real breast cancer progression. The low final error and rapid convergence time suggest the framework is both accurate and computationally efficient for clinical applications. The parameter values align with known biological constraints, particularly the competition between tumor size and structural

organization. This quantitative validation supports using the model for predicting tumor development patterns and potentially guiding treatment decisions based on individual growth characteristics. The successful fitting to clinical data shown in Fig. 14 demonstrates practical utility for modeling patient-specific tumor dynamics. The analysis of tumor growth dynamics reveals several key patterns in the evolution of tumor characteristics. As shown in Figs. 15a and 16a, the radius (R) exhibits an initial rapid growth phase followed by stabilization, with lower fractional orders (α = 0.70–0.80) demonstrating more gradual stabilization compared to higher orders (α = 0.90–0.95). This prolonged growth phase in low-α tumors may reflect the more aggressive behavior seen in certain breast cancer subtypes. The texture parameter (T) in Figs. 15b and 16b displays a consistent decreasing trend across all α values, with higher α values showing faster reduction to approximately T = 0.1 by 50 time units (5 weeks). This pattern suggests that tumors with classical growth dynamics develop more homogeneous internal structures more rapidly, while those with memory effects maintain structural irregularities for longer durations. The concavity (C) measurements in Figs. 15c and 16c show relatively stable values between 0.06 and 0.1 throughout the simulation period, with minor fluctuations being more pronounced for lower α values. This stability indicates that surface characteristics may be less sensitive to tumor growth dynamics compared to size and internal structure. The surface plots in Fig. 17 further demonstrate how these parameters evolve simultaneously with respect to both time and fractional order, revealing the complex interplay between tumor characteristics. The phase portraits provide additional insights into the relationships between these tumor features. Fig. 17a shows an inverse relationship between radius and texture, where increasing tumor size correlates with decreasing structural irregularity. This negative correlation aligns with clinical observations of larger tumors developing more homogeneous internal structures. The radius-concavity relationship in Fig. 17c demonstrates weak coupling, with concavity remaining relatively stable across different radius values. This suggests that surface deformations are governed by different biological mechanisms than those controlling tumor size. The texture-concavity relationship shown in Fig. 17b reveals nonlinear coupling, where texture dominates concavity modulation at early growth stages but becomes largely independent of structural changes beyond $T \approx 0.2$. These phase space trajectories provide valuable information about tumor development patterns, with low-α tumors maintaining higher concavity across all texture values, potentially serving as a biomarker for more aggressive subtypes. The differential responses based on α values support the utility of fractional-order modeling in capturing the spectrum of tumor behaviors observed clinically, particularly in representing the continuum from classical exponential growth to more complex, memory-dependent progression patterns seen in breast cancer. The prediction landscape in Fig. 18 illustrates our model's ability to distinguish between malignant (red) and benign (blue) cases using fractional-order dynamics with α = 0.9, revealing a nonlinear decision boundary that reflects the complex interactions between tumor size and contour irregularity. The boundary's curvature aligns with clinical knowledge, demonstrating a greater reliance on concavity for larger tumors while maintaining a robust separation of classes. Misclassified points near the transition zone correspond to diagnostically challenging borderline cases, highlighting the model's potential for clinical decision support. The α parameter's influence is evident in the boundary's shape, where higher values produce more definitive classifications compared to the conservative predictions of lower α settings. This visualization validates how fractional calculus captures both morphological features and growth history, providing an interpretable framework that bridges machine learning predictions with biological understanding of tumor progression.

Table 6: Model fitting performance

Metric	Value
Final error	0.2877

(Continued)

Table 6 (continued)

Metric	Value
Exit flag	1 (Converged)
Optimization time	14.45 s
Iterations	108
First-Order optimality	5.58×10^{-7}

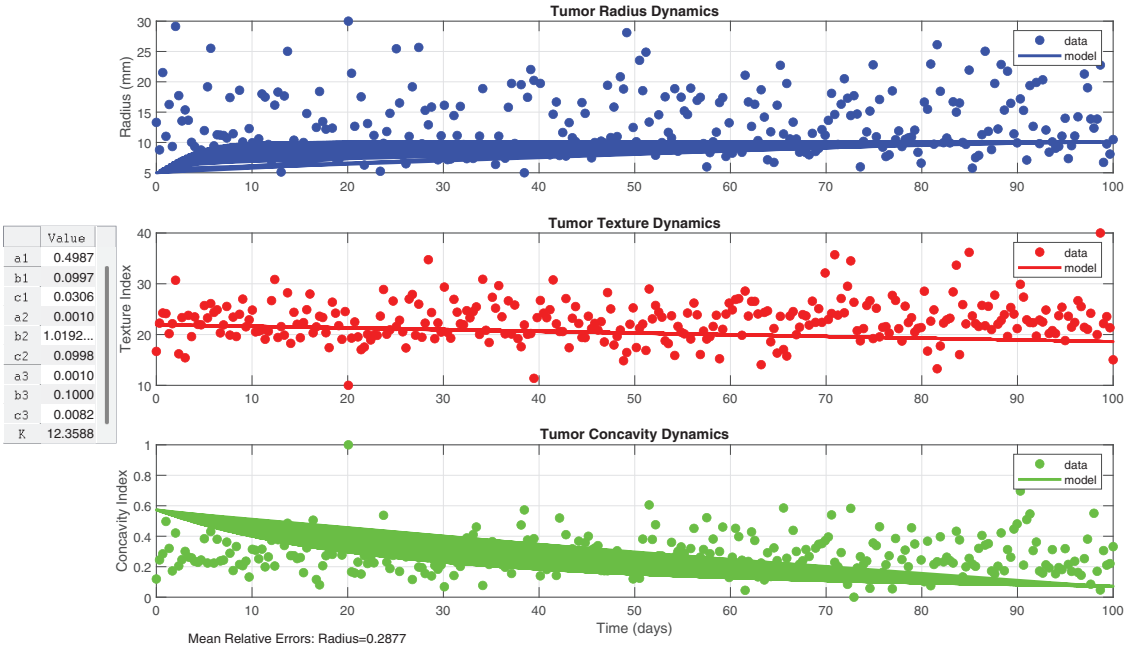

Figure 14: Model fitting to clinical data

Table 7: Optimized parameters via model fit

Parameter	Value
a_1 (Radius growth rate)	0.4987
b_1 (Radius-texture competition)	0.0997
c_1 (Radius-concavity coupling)	0.0306
a_2 (Texture growth rate)	0.0010
b_2 (Texture-radius competition)	1.0192
c_2 (Texture-concavity coupling)	0.0998
a_3 (Concavity growth rate)	0.0010
b_3 (Concavity saturation)	0.1000
c_3 (Triple interaction)	0.0082
K (Carrying capacity)	12.3588

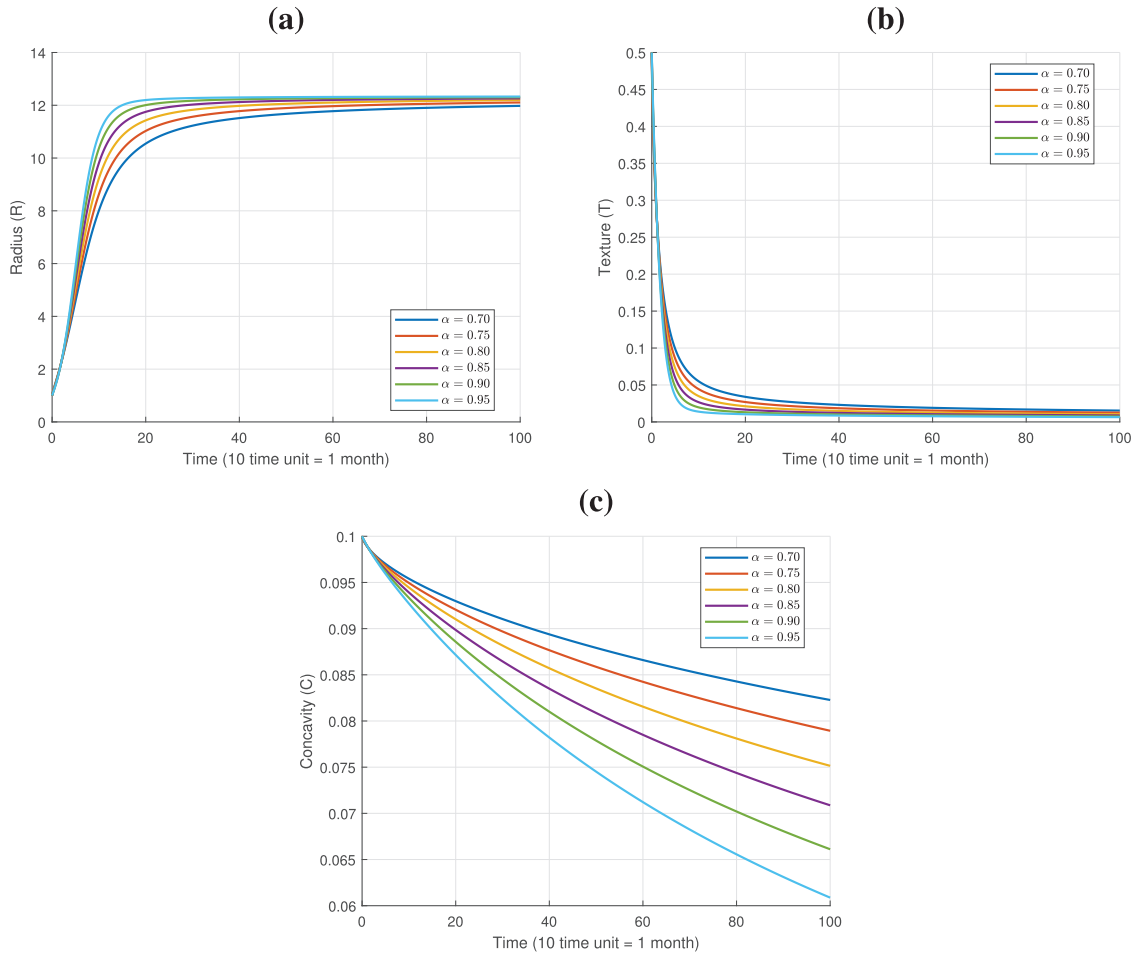

Figure 15: Two dimensional plots of the equation dynamics in model (26): **(a)** Plot of $R(t)$, **(b)** Plot of $T(t)$, and **(c)** Plot of $C(t)$

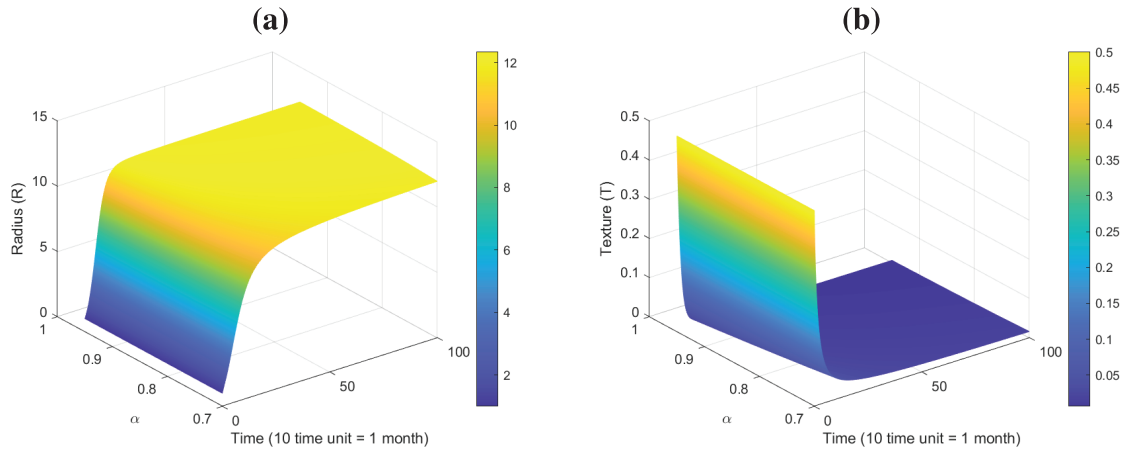

Figure 16: (Continued)

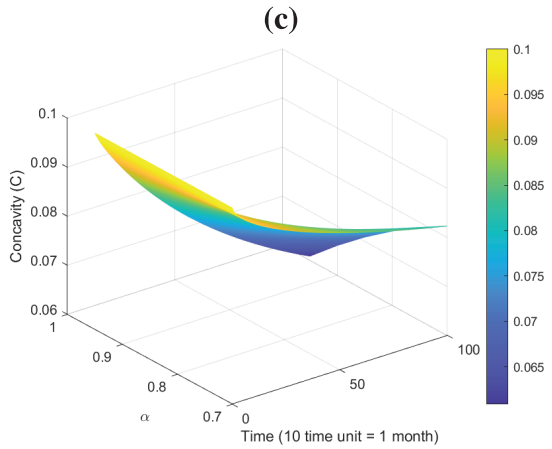

Figure 16: Surface plots dynamics of model (26): **(a)** Plot of $R(t)$, **(b)** Plot of $T(t)$, and **(c)** Plot of $C(t)$

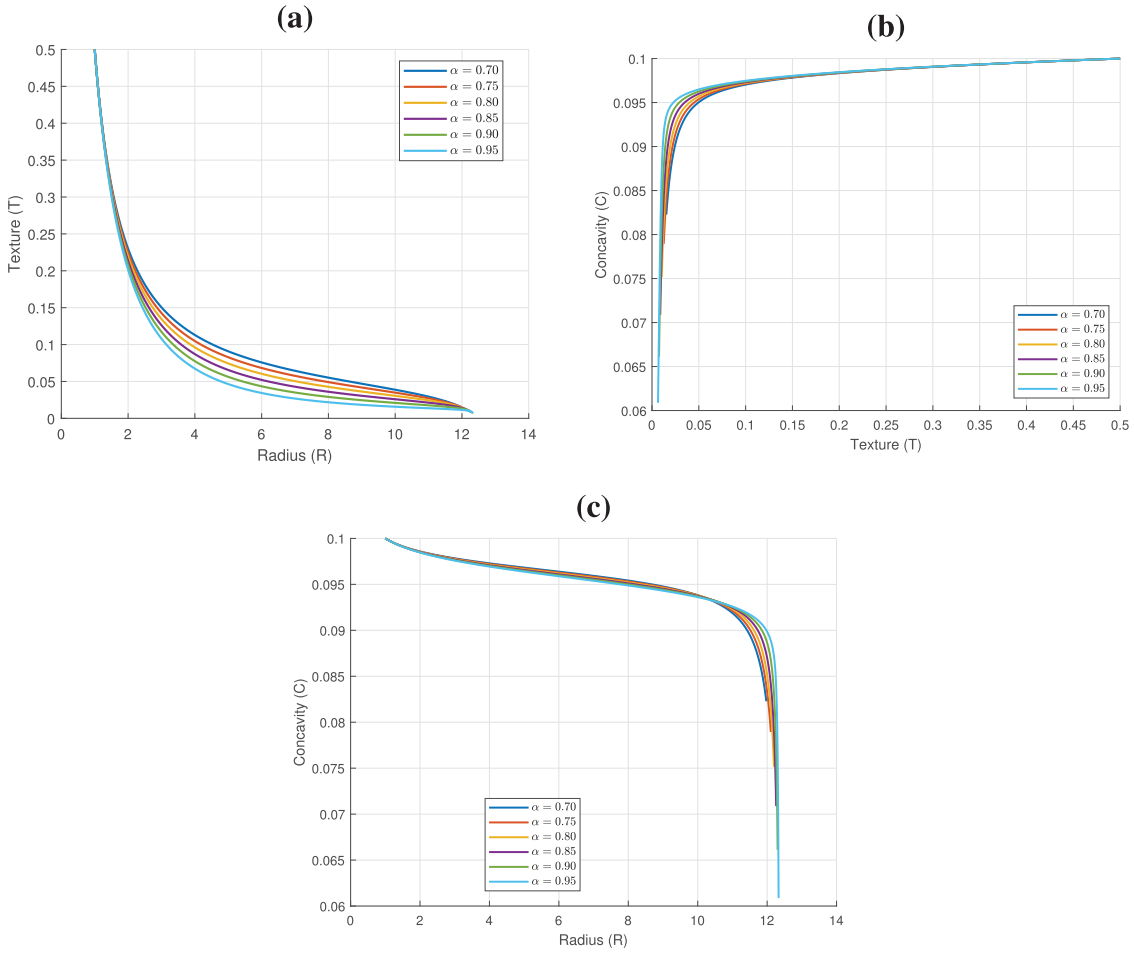

Figure 17: Phase plots of model (26): **(a)** Plot of $T(t)$ over $R(t)$, **(b)** Plot of $C(t)$ over $T(t)$, and **(c)** Plot of $C(t)$ over $R(t)$

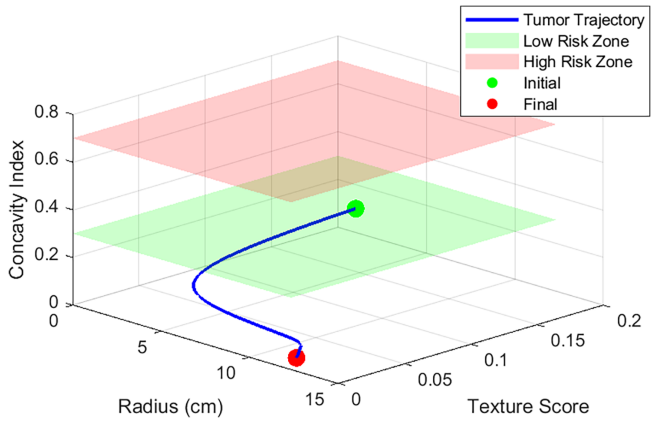

Figure 18: Malignant-benign region prediction using model (26), with $\alpha = 0.9$

6 Conclusion

This study presents a novel hybrid framework integrating machine learning and fractional-order calculus to model breast cancer progression across multiple scales. The machine learning component, evaluated on the Wisconsin Diagnostic Breast Cancer dataset, achieved exceptional diagnostic accuracy, with deep neural networks reaching 97.72% by leveraging key morphological features such as Area_worst and Radius_worst. The fractional-order dynamical model uniquely captures memory effects in tumor growth, revealing distinct temporal patterns where lower fractional orders correlate with prolonged tumor growth phases, mimicking aggressive subtypes, while higher orders reflect rapid stabilization akin to indolent tumors. The novelty of this work lies in its first-of-its-kind hybrid framework, which combines machine learning classification with fractional-order dynamics to provide both diagnostic and prognostic insights. The model enhances biological interpretability by linking parameters to clinical tumor behavior. Additionally, fractional calculus introduces memory effects, capturing long-term tumor history and offering a paradigm shift from classical integer-order models. The developed graphical user interface further enhances clinical utility by enabling real-time risk assessment, bridging the gap between theoretical modeling and practical application. Despite these advancements, certain limitations must be acknowledged. The study's data scope is currently restricted to imaging-derived features, excluding genomic and microenvironmental factors that could further refine predictions. The computational cost of deep learning models, such as the 5.3755 s per cross-validation fold required for our Deep Neural Network (DNN), could be optimized through hardware acceleration or model compression techniques. Future research directions should focus on integrating multi-omics data to enhance the fractional model's predictive power, particularly by incorporating genomic markers. Extending the framework to model therapeutic responses, such as chemotherapy effects on fractional-order values, could provide deeper clinical insights. Optimizing the graphical interface for low-resource settings through lightweight machine learning models would improve accessibility. Longitudinal studies are also needed to validate the role of memory effects, represented by α, in long-term patient outcomes. This work advances precision oncology by unifying data-driven machine learning with mechanistic modeling, offering a scalable tool for both immediate diagnosis and long-term progression tracking. Future developments could establish the fractional-order parameter α as a prognostic biomarker, guiding personalized therapeutic strategies based on tumor growth dynamics. Future studies will further validate α as a prognostic biomarker and optimize the GUI for low-resource settings."

Acknowledgement: Not applicable.

Funding Statement: The authors received no specific funding for this study.

Author Contributions: David Amilo: Conceptualization, Methodology, Data Curation, Software, Formal Analysis, and Writing, Original Draft. Khadijeh Sadri: Formal analysis, Validation, Visualization, Writing, Review, and Editing. Evren Hincal: Supervision and Project Administration, Review, and Editing. Mohamed Hafez: Supervision, Review, and Editing. All authors reviewed the results and approved the final version of the manuscript.

Availability of Data and Materials: Data used in this study are referenced within the article.

Ethics Approval: Not applicable.

Conflicts of Interest: The authors declare no conflicts of interest to report regarding the present study.

References

1. Barrios CH. Global challenges in breast cancer detection and treatment. The Breast. 2022;62(1):S3–6. doi:10.1016/j.breast.2022.02.003.
2. Trapani D, Ginsburg O, Fadelu T, Lin NU, Hassett M, Ilbawi AM, et al. Global challenges and policy solutions in breast cancer control. Cancer Treat Rev. 2022;104(3):102339. doi:10.1016/j.ctrv.2022.102339.
3. Wilkinson L, Gathani T. Understanding breast cancer as a global health concern. Br J Radio. 2022;95(1130):20211033. doi:10.1259/bjr.20211033.
4. Kim J, Harper A, McCormack V, Sung H, Houssami N, Morgan E, et al. Global patterns and trends in breast cancer incidence and mortality across 185 countries. Nat Med. 2025;31(4):1154–62. doi:10.1038/s41591-025-03502-3.
5. Xu H, Xu B. Breast cancer: epidemiology, risk factors and screening. Chin J Cancer Res. 2023;35(6):565. doi:10.21147/j.issn.1000-9604.2023.06.02.
6. Popa M-T, Noditi A, Peleaşa T-M, Stoleru S, Blidaru A. Breast cancer: a heterogeneous pathology. Prognostic and predictive factors–a narrative review. Chirurgia. 2025;120(1):32–47. doi:10.21614/chirurgia.3100.
7. Gu TQ, Xiao YL, Shao ZM. Intratumor heterogeneity in breast cancer: tracing its origins and translating findings into clinical practice. Precis Med Eng. 2024;1(1):100006. doi:10.1016/j.preme.2024.100006.
8. Shahid MS, Imran A. Breast cancer detection using deep learning techniques: challenges and future directions. Multimed Tools Appl. 2025;84(6):3257–304. doi:10.1007/s11042-025-20606-7.
9. Sharafaddini AM, Esfahani KK, Mansouri N. Deep learning approaches to detect breast cancer: a comprehensive review. Multimed Tools Appl. 2024;84(21):24079–190. doi:10.1007/s11042-024-20011-6.
10. Asif S, Yi WH, ur-Rehman S-, ul-ain Q-, Amjad K, Yi YY, et al. Advancements and prospects of machine learning in medical diagnostics: unveiling the future of diagnostic precision. Arch Comput Methods Eng. 2024;32(2):853–83. doi:10.1007/s11831-024-10148-w.
11. Rai HM, Yoo J, Razaque A. Comparative analysis of machine learning and deep learning models for improved cancer detection: a comprehensive review of recent advancements in diagnostic techniques. Expert Syst Appl. 2024;255(Part D):124838. doi:10.1016/j.eswa.2024.124838.
12. Amilo D, Sadri K, Hincal E, Farman M, Nisar KS, Hafez M. An integrated machine learning and fractional calculus approach to predicting diabetes risk in women. Healthcare Anal. 2025;8(2):100402. doi:10.1016/j.health.2025.100402.
13. Luo L, Wang X, Lin Y, Ma X, Tan A, Chan R, et al. Deep learning in breast cancer imaging: a decade of progress and future directions. IEEE Rev Biomed Eng. 2025;18:130–51. doi:10.1109/RBME.2024.3357877.
14. Darbandi MRN, Darbandi M, Darbandi S, Bado I, Hadizadeh M, Khorshid HRK. Artificial intelligence breakthroughs in pioneering early diagnosis and precision treatment of breast cancer: a multimethod study. Eur J Cancer. 2024;209:114227. doi:10.1016/j.ejca.2024.114227.
15. Orhan H, Yavşan E. Artificial intelligence-assisted detection model for melanoma diagnosis using deep learning techniques. Math Model Numer Simul Appl. 2023;3(2):159–69. doi:10.53391/mmnsa.1311943.
16. Sugiman S, Salman S, Catur AD, Asmara YP. Modelling the flexural properties of filled epoxy: effects of volume fraction. E3S Web of Conferences. 2023;465(16):01028). doi:10.1051/e3sconf/202346501028.

17. Dewi DA, Thinakan R, Batumalay M, Kurniawan TB. A model for pervasive computing and wearable devices for sustainable healthcare applications. Int J Adv Comput Sci Appl. 2023;14(10). doi:10.14569/IJACSA.2023.0141056.
18. Acay B, Inc M, Khan A, Yusuf A. Fractional methicillin-resistant Staphylococcus aureus infection model under Caputo operator. J Appl Math Comput. 2021;67(1):755–83. doi:10.1007/s12190-021-01502-3.
19. Saadeh R, Abdoon MA, Qazza A, Berir M, Guma FE, Al-Kuleab N, et al. Mathematical modeling and stability analysis of the novel fractional model in the Caputo derivative operator: a case study. Heliyon. 2024;10(5):e26611. doi:10.1016/j.heliyon.2024.e26611.
20. Bundela B, Sharma S, Singh BR. A review article on relation between mathematical modelling and machine learning. Zhongguo Kuangye Daxue Xuebao. 2024;29(2):123–9.
21. Amilo D, Izuchukwu C, Sadri K, Yao HR, Hincal E, Shehu Y. A fractional-order model for optimizing combination therapy in heterogeneous lung cancer: integrating immunotherapy and targeted therapy to minimize side effects. Sci Rep. 2024;14(1):18484. doi:10.1038/s41598-024-66531-x.
22. Xu C, Farman M, Pang Y, Liu Z, Liao M, Yao L, et al. Mathematical analysis and dynamical transmission of (SEIrIsR) model with different infection stages by using fractional operator. Int J Biomath. 2024. doi:10.1142/S1793524524501511.
23. Ucar S, Koca I, Özdemir N, Inci T. A stochastic approach to tumor modeling incorporating macrophages. Bull Biomath. 2024;2(2):162–81. doi:10.59292/bulletinbiomath.2024007.
24. Amilo D, Sadri K, Kaymakamzade B, Hincal E. A mathematical model with fractional-order dynamics for the combined treatment of metastatic colorectal cancer. Commun Nonlinear Sci Numer Simul. 2024;130(7):107756. doi:10.1016/j.cnsns.2023.107756.
25. Amilo D, Sadri K, Farman M, Hincal E, Nisar KS. New insights into disease dynamics and treatment interventions with PID controller-based therapeutic strategies for pancreatic cancer. Comput Math Appl. 2025;181(1):133–62. doi:10.1016/j.camwa.2025.01.006.
26. Amilo D, Kaymakamzade B, Hincal E. A fractional-order mathematical model for lung cancer incorporating integrated therapeutic approaches. Sci Rep. 2023;13(1):12426. doi:10.1038/s41598-023-38814-2.
27. El-Sayed AA, Baleanu D, Agarwal P. A novel Jacobi operational matrix for numerical solution of multi-term variable-order fractional differential equations. J Taibah Univ Sci. 2020;14(1):963–74. doi:10.1080/16583655.2020.1792681.
28. Agarwal P, El-Sayed AA, Tariboon J. Vieta-Fibonacci operational matrices for spectral solutions of variable-order fractional integro-differential equations. J Comput Appl Math. 2021;382(2):113063. doi:10.1016/j.cam.2020.113063.
29. Swain S, Swain S, Panda B, Tripathy MC. Modeling and optimal analysis of lung cancer cell growth and apoptosis with fractional-order dynamics. Comput Biol Med. 2025;188(11):109837. doi:10.1016/j.compbiomed.2025.109837.
30. Karaca Y. Computational complexity-based fractional-order neural network models for the diagnostic treatments and predictive transdifferentiability of heterogeneous cancer cell propensity. Chaos Theory Appl. 2023;5(1):34–51. doi:10.51537/chaos.1249532.
31. Vieira LC, Costa RS, Valério D. An overview of mathematical modelling in cancer research: fractional calculus as modelling tool. Frac Fraction. 2023;7(8):595. doi:10.3390/fractalfract7080595.
32. Behinfaraz R, Ghavifekr AA, De Fazio R, Visconti P. Utilizing fractional artificial neural networks for modeling cancer cell behavior. Electronics. 2023;12(20):4245. doi:10.3390/electronics12204245.
33. Nagdeote S, Prabhu S. A model to perform prediction based on feature extraction of histopathological images of the breast. Multimed Tools Appl. 2024;83(6):18119–46. doi:10.1007/s11042-023-16245-5.
34. Imam S, Aijaz M, Iffat W, Jamshed SQ, Ismail NE, Paneerselvam GS, et al. Attitudes and understanding of complementary and alternative medicine in cancer care: an exploratory study of patients' perspectives in Karachi. Pakistan Asian Pac J Trop Med. 2023;16(9):400–8. doi:10.4103/1995-7645.386075.
35. Al-Dhabyani W, Gomaa M, Khaled H, Fahmy A. Dataset of breast ultrasound images. Data Brief. 2020;28(5):104863. doi:10.1016/j.dib.2019.104863.
36. Wolberg W, Mangasarian O, Street N, Street W. Breast cancer wisconsin (Diagnostic) [Dataset]. UCI Machine Learning Repository. 1993. doi:10.24432/C5DW2B.

37. Singh LK, Khanna M, Singh R. An enhanced soft-computing based strategy for efficient feature selection for timely breast cancer prediction: Wisconsin Diagnostic Breast Cancer dataset case. Multimed Tools Appl. 2024;83(31):76607–72. doi:10.1007/s11042-024-18473-9.
38. Sadeghi-Lotfabadi A, Ghiasi-Shirazi K. Speeding up L-BFGS by direct approximation of the inverse Hessian matrix. Comput Optim Appl. 2025;91(1):283–310. doi:10.1007/s10589-025-00665-0.
39. So AMC, Zhou Z. Non-asymptotic convergence analysis of inexact gradient methods for machine learning without strong convexity. Optim Methods Softw. 2017;32(4):963–92. doi:10.1080/10556788.2017.1296439.
40. Valentim Junior CA. Fractional mathematical oncology: cancer-related dynamics under an interdisciplinary viewpoint [doctoral dissertation]. Brazil: São Paulo; 2023. doi:10.11606/T.74.2023.tde-07112023-093919.
41. Jiang G, Gao X, Huang R, Wu C. Fractional-Order RNNs: a universal approximation framework for non-local dynamic system modeling. IEEE Trans Signal Process. 2025. doi:10.1109/TSP.2025.3585881.
42. Abu-Shady M, Kaabar MK. A generalized definition of the fractional derivative with applications. Math Probl Eng. 2021;2021(1):9444803. doi:10.1155/2021/9444803.
43. Amilo D, Sadri K, Hincal E. Comparative analysis of caputo and variable-order fractional derivative algorithms across various applications. Int J Appl Comput Math. 2025;11(3):80. doi:10.1007/s40819-025-01887-w.
44. Sadri K, Amilo D, Hinçal E. A combination of classical and shifted Jacobi polynomials for two-dimensional time-fractional diffusion-wave equations. Chaos Solitons Fractals. 2025;198:116569. doi:10.1016/j.chaos.2025.116569.
45. Lin SY. New results for generalized Gronwall Inequalities and their applications. Abstr Appl Anal. 2014;2014:168594. doi:10.1155/2014/168594.